

Magnetoelastic Coupling and Phases in the Skyrmion Lattice Magnet Gd_2PdSi_3 Discovered by High-resolution Dilatometry

S. Spachmann^{1,*}, A. Elghandour¹, M. Frontzek^{2,4}, W. Löser³, and R. Klingeler^{1,4}

¹*Kirchhoff Institute for Physics, Heidelberg University, Germany*

²*Oak Ridge National Laboratory, Oak Ridge, USA*

³*Leibniz Institute for Solid State and Materials Research (IFW), Dresden, Germany*

⁴*Institute of Solid State and Materials Physics,
Dresden University of Technology, Germany and*

⁴*Centre for Advanced Materials (CAM), Heidelberg University, Germany*

(Dated: April 28, 2021)

Abstract

We report detailed thermodynamic studies on high-quality single crystals of the centrosymmetric skyrmion-hosting intermetallic Gd_2PdSi_3 by means of high-resolution capacitance dilatometry in fields up to 15 T which are complemented by specific heat and magnetization studies. Our dilatometric measurements show magnetoelastic effects associated with antiferromagnetic order at $T_{\text{N}1} = 22.3$ K and $T_{\text{N}2} = 19.7$ K, as well as strong field effects in an applied magnetic field of 15 T up to 200 K (150 K) for $B \parallel c$ ($B \parallel a^*$, i.e. $B \perp c$). The data allow us to complete the magnetic phase diagram, including a new feature at $T^* \approx 12$ K below which a new degree of freedom becomes relevant. For the first time, the magnetic B vs. T phase diagram for the a^* -axis is also reported. Grüneisen analysis shows the onset of magnetic contributions around 60 K, i.e., well above $T_{\text{N}1}$. Uniaxial pressure dependencies of opposite sign, -1.3 K/GPa and 0.3 K/GPa, are extracted for the out-of-plane and in-plane directions at $T_{\text{N}1}$. For T^* we obtain $\partial T^*/\partial p_c = 1.4$ K/GPa. In particular we elucidate thermodynamic properties of the recently discovered skyrmion lattice phase and show that it is strongly enhanced by uniaxial pressure.

I. INTRODUCTION

Ternary intermetallic compounds of the type R_2TX_3 (R = rare earth, T = transition metal, X = element of main groups III to V)^{1,2} have been investigated extensively over the past decades, due to their variety of intriguing electronic properties ranging from superconductivity³, giant magnetoresistance (GMR)⁴⁻⁶, ferromagnetism⁷ and incommensurate spin structures^{8,9}, phenomena related to Kondo physics and heavy fermions¹⁰⁻¹², to non-Fermi-liquid¹⁰ and spin-glass behavior¹³⁻¹⁶. This is particularly evident in the title material Gd_2PdSi_3 where a skyrmion lattice phase featuring giant topological Hall and Nernst effect was discovered recently.^{8,17,18}

Most members of the R_2PdSi_3 family of ternary silicides crystallize in a highly symmetric AlB_2 -derived hexagonal structure (space group $P6/mmm$) with triangular lattice layers of R^{3+} magnetic sites sandwiching honeycomb nets of Pd/Si sites. While the Pd and Si ions were originally believed to be distributed statistically¹⁹, an X-ray and neutron diffraction study by Tang et al. showed for Ho_2PdSi_3 that these ions actually order into a superstructure along both in- and out-of-plane directions, while the overall centrosymmetry of the structure is retained²⁰. This leads to two nonequivalent sites for the R^{3+} ions, which has been shown to affect the magnetism in an applied magnetic field for Er_2PdSi_3 ²¹. While no structural phase transition has been detected for $R = Gd, Tb, Dy, Ho, Er$ and Tm , most R_2PdSi_3 compounds show long-range magnetic order at low temperatures²²⁻²⁴.

These various ordering phenomena are driven by a delicate interplay of indirect exchange coupling mediated by the conduction electrons, i.e., the Rudermann-Kittel-Kasuya-Yosida (RKKY) interaction, spin-orbit coupling and the influence of crystal field (CF) effects. The Gd^{3+} ions in Gd_2PdSi_3 , however, with a half-filled $4f$ shell, have vanishing orbital momentum ($\mathbf{J} \approx \mathbf{S} = 7/2$) and are not influenced by crystal field effects. Magnetic order, therefore, arises from the RKKY interaction and dipole-dipole interactions. Gd_2PdSi_3 exhibits two successive phase transitions around $T_N = 21$ K⁹ and was found to exhibit a skyrmion lattice (SkL) phase of Bloch-type skyrmions in low magnetic fields applied along the c -axis⁸. A number of incommensurate spin structures both in zero-field as well as in higher applied magnetic fields have been identified⁹ and the phase diagram in fields up to 9 T has been established through resistance and magnetization measurements as well as resonant X-ray scattering^{8,9,22,25}. Single crystal X-ray and neutron diffraction measurements yielded lattice

parameters at 300 K (2 K) of $a = 4.079 \text{ \AA}$ (4.066 \AA) and $c = 4.098 \text{ \AA}$ (4.091 \AA), i.e. $\Delta a/a = 3.2 \cdot 10^{-3}$ and $\Delta c/c = 1.7 \cdot 10^{-3}$.^{20,26}

Except for these measurements of the lattice parameters, however, there is at present no study on magnetoelastic effects in Gd_2PdSi_3 . Therefore, with a particular focus on the skyrmion lattice phase, we report detailed dilatometric studies of Gd_2PdSi_3 in a wide range of temperatures and magnetic fields. Our thermal expansion and magnetostriction data show pronounced magnetoelastic coupling and field effects extending up to temperatures of 150 K and above. Moreover, we uncover yet unreported phases and an anomaly in zero-field which appears well below the Néel transitions at $T_{\text{N1}} = 22.3(5) \text{ K}$ and $T_{\text{N2}} = 19.7(5) \text{ K}$, thereby evidencing competing interactions already in zero-field. We update the magnetic phase diagram for $B \parallel c$ -axis, present for the first time the phase diagram for $B \parallel a^*$ -axis, and discuss in detail the thermodynamic properties for $B \parallel c$. Our results in particular elucidate the skyrmion lattice phase and we show that it is enhanced by uniaxial pressure.

II. EXPERIMENTAL METHODS

Single crystals of Gd_2PdSi_3 have been grown by the optical floating-zone method as reported in Ref. [27,28] and were previously studied by AC susceptibility, neutron diffraction²², and angle-resolved photoemission spectroscopy²⁹. The magnetization was studied in the temperature regime from 1.8 K to 300 K in magnetic fields up to 7 T in a Magnetic Properties Measurement System (MPMS3, Quantum Design) and up to 14 T in a Physical Properties Measurement System (PPMS, Quantum Design) using the Vibrating Sample Magnetometry (VSM) option. Specific heat measurements were performed on a PPMS-14 using a relaxation method on single crystals of $m = 20.79 \text{ mg}$ (2 K-300 K) and 13.49 mg (0.15 K-3 K). High-resolution dilatometry measurements were performed by means of a three-terminal high-resolution capacitance dilatometer in a home-built setup placed inside a Variable Temperature Insert (VTI) of an Oxford magnet system^{30,31}. With this dilatometer, the relative length changes dL_i/L_i along the crystallographic c and a^* directions, respectively, were studied on an oriented cuboid-shaped single crystal of dimensions $2.480 \times 1.300 \times 1.459 \text{ mm}^3$. Measurements were performed at temperatures between 2 K and 300 K in magnetic fields up to 15 T, applied along the direction of the measured length changes, and the linear thermal expansion coefficients $\alpha_i = 1/L_i \cdot dL_i(T)/dT$ were derived. In addition, the field-

induced length changes $dL_i(B_i)$ were measured at various fixed temperatures between 1.7 K and 200 K in magnetic fields up to 15 T. The longitudinal magnetostriction coefficient $\lambda_i = 1/L_i \cdot dL_i(B_i)/dB_i$ was derived from $dL_i(B_i)$.

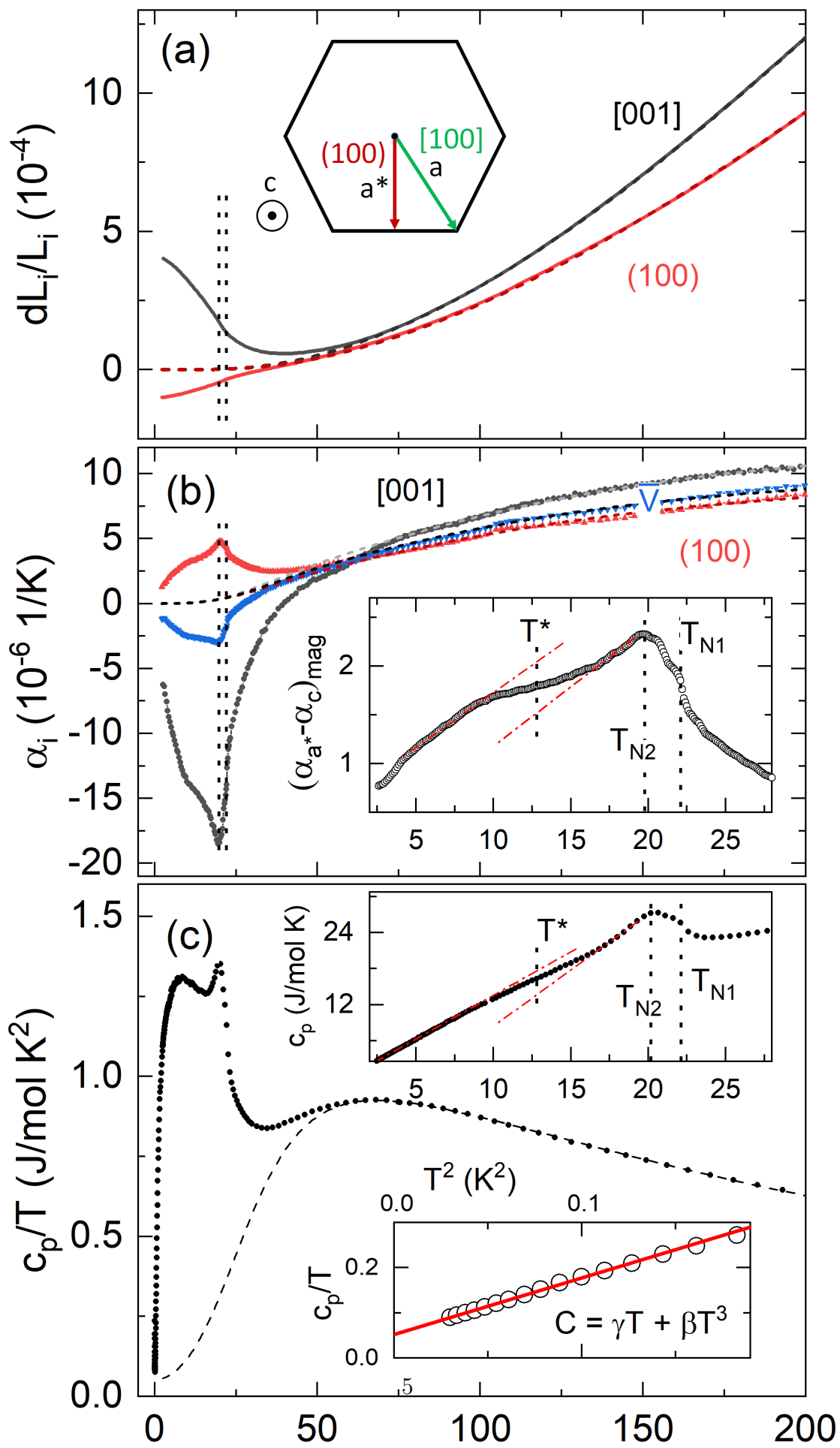
III. EXPERIMENTAL RESULTS

A. Evolution of magnetic order at $B = 0$

Uniaxial thermal expansion and specific heat show pronounced anomalies around 20 K which are associated with the onset of long-range magnetic order (Fig. 1). Close inspection of the anomalies indicates the proximity of not only one, but two phase transitions around T_N . While the anomaly at $T_{N1} = 22.3(5)$ K is seen as a jump in α_i , the anomaly at $T_{N2} = 19.7(5)$ K (20.3(5) K for the a^* -axis) is expressed as a peak. This observation confirms the results by Hirschberger et al. of two consecutive phase transitions in zero field⁹. Beyond these two known transitions, however, our data display a third anomaly indicative of a phase transition which has not been reported for single crystals of Gd_2PdSi_3 . This anomaly, marked by $T^* \approx 13$ K in the inset of Fig. 1(b), is visible as a broad jump for both directions in α_i which extends between 10 K and 15 K and will be discussed in more detail below.

The specific heat data show the three observed features at T_{N1} , T_{N2} and T^* , too (Fig. 1(c)). The shape of the anomalies in c_p is analogous to their shape in α_{a^*} . At very low temperatures below about 400 mK a quasi-linear behavior of c_p/T vs. T^2 is found (see the inset of Fig. 1(c)) reminding of similar observations in Lu_2PdSi_3 and Ce_2PdSi_3 .^{11,32} In this temperature regime, the data are described well by a linear and a cubic term, i.e., $c_p/T = \gamma + \beta T^2$. The quasi-linear term is described by an effective Sommerfeld coefficient $\gamma = 52(5)$ mJ/(mol K^2). This parameter is in between the values obtained for Lu_2PdSi_3 (6.9 mJ/(mol K^2)) and Ce_2PdSi_3 (108 mJ/(mol K^2)), the latter being discussed as evidence of heavy-fermion behaviour.¹¹ Whereas phonons can be neglected in this temperature regime, the coefficient $\beta = 1.25(3)$ J/(mol K^4) is rather large and reflects the contribution of low-energy antiferromagnetic excitations.

The dashed lines in Fig. 1 show the phononic and electronic contributions to the relative length changes, thermal expansion coefficients, and specific heat. In order to obtain these contributions, the specific heat of the non-magnetic analog Lu_2PdSi_3 as reported by Cao



et al.³² was fitted by phononic Debye and Einstein terms, as well as an electronic term, according to

$$c_p^{el,ph} = \gamma T + n_D D\left(\frac{T}{\Theta_D}\right) + n_E E\left(\frac{T}{\Theta_E}\right) \quad (1)$$

where γ is the Sommerfeld coefficient, n_D and n_E are constants, $D(T/\Theta_D)$ and $E(T/\Theta_E)$ are the Debye and Einstein functions with the Debye and Einstein temperatures Θ_D and Θ_E . The fit to the Lu_2PdSi_3 specific heat data yields $\Theta_D = 213$ K, $\Theta_E = 454$ K, with $n_D = 3.69$ and $n_E = 1.98$. γ was fixed to the value reported by Cao et al. of 6.93 mJ/(mol K²). Compared to $\Theta_D = 191$ K by Cao et al., extracted from the low temperature regime, our value is slightly larger.

Scaling the Debye and Einstein temperatures by the different masses of Lu and Gd we obtain a scaling factor³³ of $\Theta_{D,LPS}/\Theta_{D,GPS} = 0.962$. The specific heat and thermal expansion of Gd_2PdSi_3 were thus fitted with fixed $\Theta_D = 222$ K = $\Theta_{D,LPS}/0.962$ and correspondingly $\Theta_E = 471$ K. For the fit to the specific heat, $\gamma = 52$ mJ/(mol K²) was also fixed. For the thermal expansion the electronic contribution was negligibly small and therefore omitted, i.e. it was fitted by

$$\alpha^{ph} = n_D D\left(\frac{T}{\Theta_D}\right) + n_E E\left(\frac{T}{\Theta_E}\right) \quad (2)$$

with parameters n_D and n_E . The phononic contributions to dL_i/L_i in Fig. 1(a) were obtained by integrating the background obtained for the respective α_i .

Subtracting the electronic and phononic backgrounds from the specific heat and thermal expansion coefficients yields their respective magnetic contributions which extend up to about 60 K. This agrees with the temperature regime where the magnetization exhibits a non-linear field dependence up to 7 T (see Fig. S1). From $c_{p,mag}/T$ the changes in magnetic entropy, S_{mag} , above 150 mK are calculated. We obtain a constant $\Delta S_{mag}(T > 150 \text{ mK}) = 31.3$ J/(mol K) above 60 K, which is 90% of the full expected magnetic entropy of $2R \ln 8 = 34.6$ J/(mol K), where R is the universal gas constant.

Returning to the thermal expansion data, we see that the anomalies in the thermal expansion coefficients, at T_{N1} and T_{N2} , are of opposite sign for the c - and a^* -axis, indicating opposite pressure dependencies $\partial T_{Ni}/\partial p_c < 0$ and $\partial T_{Ni}/\partial p_{a^*} > 0$. The volume thermal expansion also indicates a negative hydrostatic pressure dependence $\partial T_{Ni}/\partial p < 0$ for both antiferromagnetic transitions.

The Grüneisen ratio of the thermal expansion coefficient and the specific heat is a valuable quantity to determine the relevant energy scales driving the system and to quantify its pressure dependencies. In the presence of one dominant energy scale ϵ , this ratio is independent of temperature and enables the determination of the pressure dependence of ϵ , i.e. ^{34,35},

$$\Gamma_i = \frac{\alpha_i}{c_p} = \frac{1}{TV_m} \frac{\partial S / \partial p_i}{\partial S / \partial T} = \frac{1}{V_m} \frac{\partial \ln \epsilon}{\partial p_i}. \quad (3)$$

Here, V_m is the molar volume and the index i indicates a linear direction or the volume. At T_N , Eq. 3 converts to $\Gamma = (T_N V_m)^{-1} \cdot \partial T_N / \partial p$. Comparing the magnetic contributions $\alpha_{i,\text{mag}}$ and $c_{p,\text{mag}}$ hence allows to identify temperature regimes where the Grüneisen relation implies only one dominant energy scale while appropriate scaling enables to read off the respective parameter $\Gamma_{i,\text{mag}}$. As shown in Fig. 2, the overall behavior of $\alpha_{i,\text{mag}}$ and $c_{p,\text{mag}}$ is similar except for a distinct jump in $\alpha_{i,\text{mag}}$ at ~ 12 K which is much less pronounced in the magnetic specific heat. In both cases, magnetic contributions start to evolve around 60 K.

Despite the overall similar behavior, there are differences at higher temperatures, too. While the a^* -axis shows a nearly perfect overlap between $\alpha_{i,\text{mag}}$ and $c_{p,\text{mag}}$ down to 14 K as shown in Fig. 2(a), we only observe a very good agreement around T_{N1} and T_{N2} for the c -axis, in a range from 17 K to about 23 K. We also note that below ~ 14 K our results indicate the failure of Grüneisen scaling rather than the presence of just a different scaling parameter.

Our data, however, clearly imply the presence of a single dominant energy scale at and around the magnetic ordering temperatures T_{N1} and T_{N2} . The obtained Grüneisen parameters amount to $\Gamma_{c,\text{mag}} = -91(13) \cdot 10^{-8}$ mol/J and $\Gamma_{a^*,\text{mag}} = 22(3) \cdot 10^{-8}$ mol/J. From these values, moderate pressure dependencies are derived, i.e., we obtain negative pressure dependencies $\partial T_{N1} / \partial p_c = -1.3(2)$ K/GPa and $\partial T_{N2} / \partial p_c = -1.4(2)$ K/GPa for uniaxial pressure applied along the c -axis. The uniaxial pressure dependencies for $p \parallel a^*$ -axis are positive and more than a factor of four smaller, i.e., 0.31(5) K/GPa for T_{N1} and 0.34(5) K/GPa for T_{N2} .

While our data hence evidence that the ordering phenomena at T_{N1} and T_{N2} are governed by the same energy scale, an additional energy scale becomes relevant upon further cooling, around T^* , as proven by the failure of Grüneisen scaling (cf. Fig. 2). Closer inspection of the associated anomalies implies not only a broad jump-like increase in the thermal expansion coefficients but also a less pronounced anomaly in c_p which is visible much more clearly in the

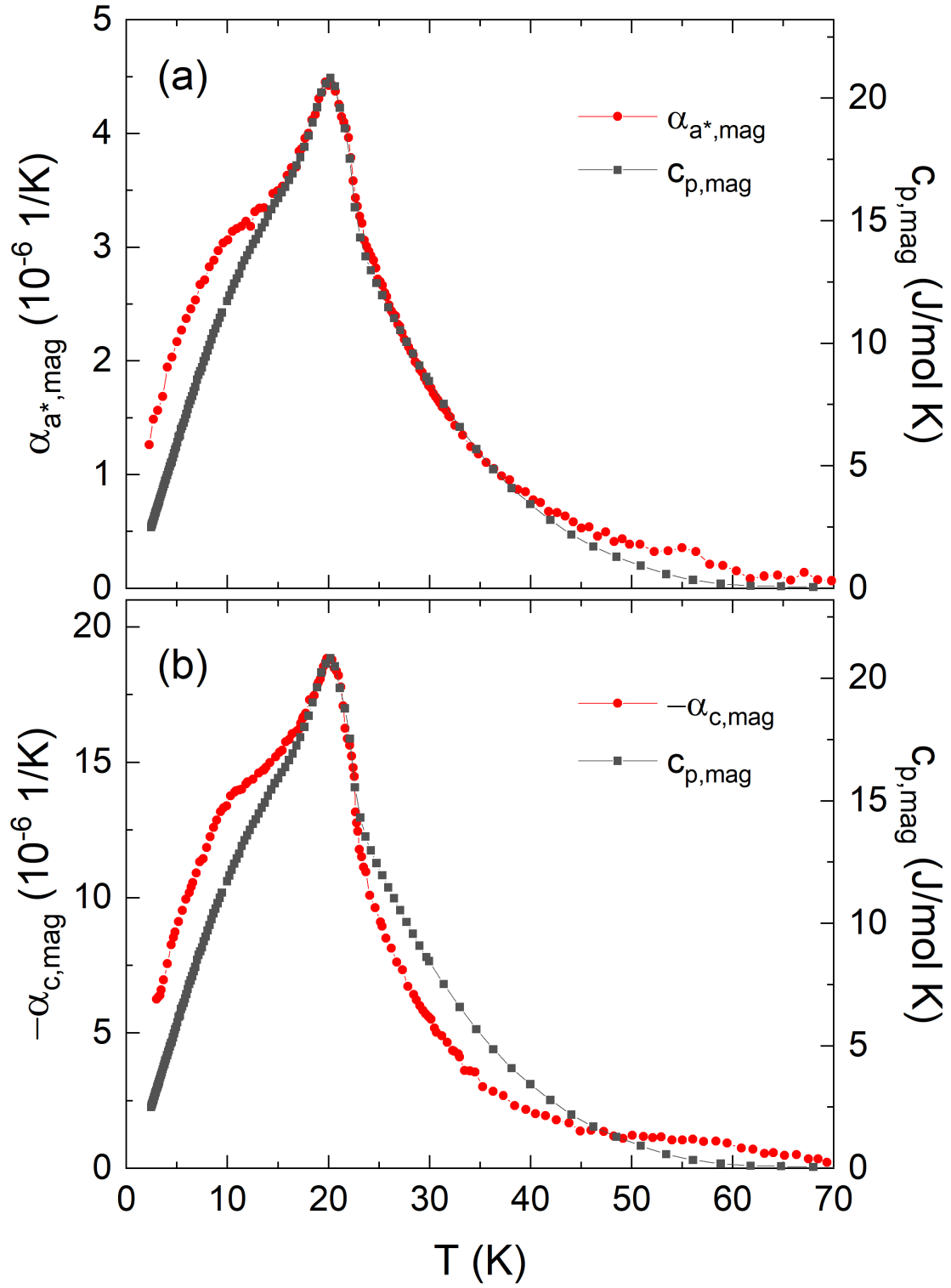


Figure 2: Magnetic contributions to the thermal expansion coefficient (left axis) and specific heat (right axis) for (a) the a^* -axis and (b) the c -axis after subtracting phononic and electronic contributions as described in the text.³⁶

c_p/T data in Fig. 1c. In an attempt to deduce the anomaly size associated with the respective features we obtain $\Delta c_p^* \approx 2.7(5)$ J/(mol K), $\Delta\alpha_v^* \approx 1.8 \cdot 10^{-6}/\text{K}$, $\Delta\alpha_c^* \approx 4.1(6) \cdot 10^{-6}/\text{K}$, $\Delta\alpha_a^* \approx -1.0(3) \cdot 10^{-6}/\text{K}$. The changes in magnetization around T^* are very small for both axes and could not be seen in the isothermal magnetization $M(B)$. However, temperature sweeps of the magnetization in static field evidence a jump in $\partial\chi/\partial T$, which is visible for $B \geq 0.2$ T (0.25 T) for $B \parallel c$ ($B \parallel a^*$) (see SI, Fig. S10(a)). At 0.2 T the jump height amounts to $5.6(1.4) \cdot 10^{-3} \mu_B/(\text{f.u. K})$. Further values are listed in Tab. S7.

B. Thermal Expansion at $B \neq 0$ and Magnetostriction

The effect of high magnetic fields on the thermal expansion and specific heat is shown in Fig. 3. A number of observations can be made: (1) The sharp features indicating phase transitions are absent at $B = 15$ T. (2) Significant entropy is shifted to higher temperatures and, at $B = 15$ T, significant field effects are visible at least up to 150 K in all shown quantities, in particular for α_c even up to about 200 K. (3) Magnetostriction from 0 T to 15 T is positive (negative) for the c -axis (a^* -axis), and (4) the temperature region of negative thermal expansion of the c -axis extends up to about 65 K at 15 T, compared to 38 K in zero-field. Note, that the magnetostriction data fully agree to the thermal expansion data at $B \neq 0$ T as shown by the (green) vertical lines in the inset of Fig. 3).

Magnetostriction data at $T \approx 2$ K shown in Fig. 4(a) and (d) further confirm strong magnetoelastic coupling and in addition clearly show the field-induced phase transitions. For comparison the isothermal magnetic susceptibility $\chi(B) = \partial M(B)/\partial B$ is also presented on the same field scale for both directions (Fig. 4(b-c)). Considering the data for $B \parallel c$, four anomalies can be identified (Fig. 4(a)): Up to 3.5 T, there are two sharp peaks in λ_c signalling jumps in $dL_c(B)$ with only small field-hysteresis, followed by a broad peak with a large hysteresis of ~ 0.8 T. The size of the anomalies for up- and down-sweep differs strongly. All three anomalies indicate discontinuous phase transitions. Corresponding anomalies and hystereses are also visible in the magnetic susceptibility. In addition, there is a broad downward jump in λ_c at around 9 T, above which magnetostriction becomes virtually zero which is also reflected by small χ , i.e., rather full alignment of magnetic moments in field (please note the logarithmic scale in Fig. 4(b) and (c)). The overall region where hysteresis is visible extends from about 6 T down to the lowest fields (see the inset in Fig. 4(a))

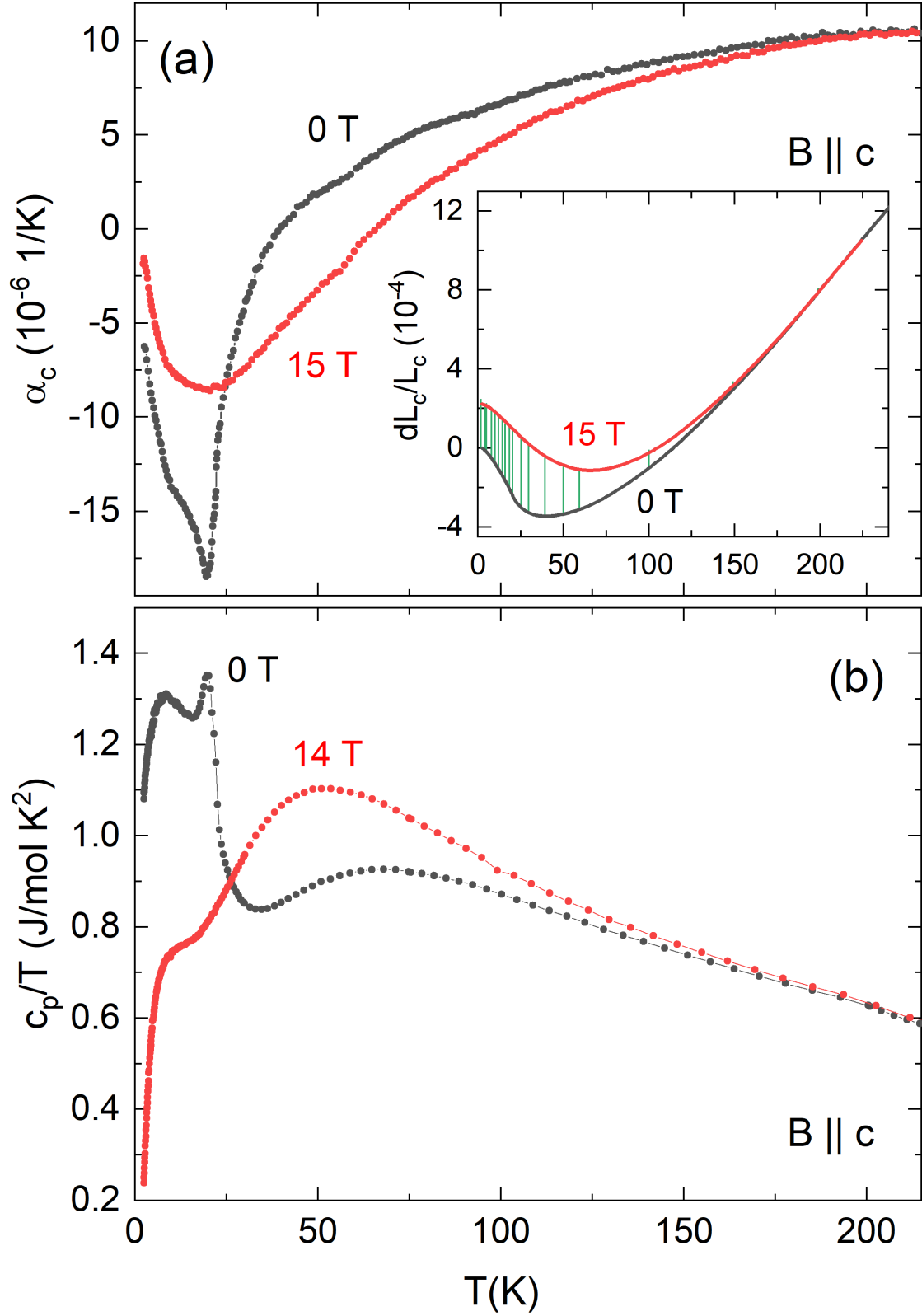


Figure 3: The effect of high fields on (a) the thermal expansion coefficient ($B = 15 \text{ T}$) and (b) the specific heat c_p/T ($B = 14 \text{ T}$) as compared to zero-field measurements. The inset in (a) shows the relative length changes. Vertical green bars indicate magnetostriction data from 0 T to 15 T at several temperatures.

but no remanent magnetostriction is visible which would indicate irreversible changes in the sample, e.g., through domain effects. Four features are also visible in λ_{a^*} for $B \parallel a^*$ (Fig. 4(d)). These anomalies are smaller in magnitude, much broader and less well-defined than for the c -axis. Similar to the findings for $\lambda_c(B \parallel c)$, there is a jump at higher fields, at about 7.3 T, but here of opposite sign. Again, it signals a continuous transition to the saturated phase of vanishing magnetostriction. In contrast to $B \parallel c$, the magnetostriction measurements $dL_{a^*}(B \parallel a^*)$ feature pronounced remanent magnetostriction below 5 K, i.e., non-zero overall length changes after sweeping the field from 0 T to 15 T and back to 0 T. At 1.8 K, this amounts to $(\Delta L/L)_{\text{rem}} = 1.4 \cdot 10^{-5}$. We attribute this observation to the irreversible effects of structural or magnetic domains as seen, e.g., in CoCl_2 ³⁷, NiCl_2 ³⁸ and NiTiO_3 ³⁹. Such irreversible domain effects seem to be absent in the measurements along the c -axis. The transition between a multidomain and single domain state may thus be fully reversible for $B \parallel c$. We conclude that hysteresis found for $B \parallel a^*$ below 3.5 T is both due to the discontinuous nature of the phase transitions and domain effects.

Both data sets, hence, imply a series of four phase transitions in magnetic field, at $T \approx 2$ K, which is also corroborated by magnetization studies (also see Fig. S7) and agrees to the recently published phase diagram for $B \parallel c$.⁹ Following the notations in Refs. [8, 9] for the phases appearing for $B \parallel c$, we label the respective phases as IC-1, A, IC-2, DP, and field induced ferromagnetic (fiFM) phase, with IC-1/IC-2 being characterized by incommensurate spin configurations, A by the formation of a skyrmion lattice (SkL), and DP by the depinning of the direction of magnetic moments (see also the phase diagram in Fig. 6). We note, however, that while the magnetostriction data evidence field-driven structural changes, domain effects may obscure the actual phase transitions up to the field and temperature regions at which a single domain state is achieved. In particular, broad peaks in the magnetostriction coefficients as seen in λ_{a^*} (Fig. 4(b), S4(e) and (f)) do not necessarily indicate the actual phase boundaries, but the peak positions may differ from those found in the magnetization studies, as shown by a phenomenological model by Kalita et al.³⁷. Therefore, for the further thermodynamic analysis of the phase boundaries as well as the construction of the phase diagram, for $B \parallel a^*$ we will only consider anomalies in the magnetostriction which can directly be linked to anomalies in isothermal magnetization.

In order to obtain the phase boundaries, we have performed thorough magnetostriction and isothermal magnetization studies at various fixed temperatures as well as corresponding

temperature sweeps at fixed magnetic field (see Figs. S4, S5, S7).⁴¹ This is demonstrated in Fig. 5, where the thermal expansion coefficients in low fields up to 3 T and the corresponding magnetization data are presented. For $B \parallel c$ (Fig. 5(a) and (b)), the evolution of two different phase boundaries can be traced straightforwardly. Specifically, applying small fields yields a suppression of T_{N2} while the jump at T_{N1} becomes more distinguished. In increasing field T_{N1} is also suppressed to lower temperature, but to a smaller extent (Fig. 5a). Above 0.3 T the peak assigned to T_{N2} at zero-field changes its shape, signaling the transition from the previously reported skyrmion lattice A phase to the IC-2 phase. It is associated with a jump $\Delta\chi_c^A$ in the static susceptibility from one T -independent value to another (Fig. 5(b)). At 0.4 T, a second feature corresponding to the transition from the A phase to the IC-1 phase is visible in both α_c and χ_c , while above 0.9 T (1 T for χ_c) all features below T_{N1} are gone. Quantitatively, $\Delta\chi_c^A$ gradually decreases from $0.91 \mu_B/\text{Gd}^{3+}$ at 0.9 T and 8.6 K to $0.36 \mu_B/\text{Gd}^{3+}$ at 0.4 T and 16.4 K. The pronounced jump in α_c at T_{N1} corresponds to a kink in the static susceptibility, i.e., a jump in its derivative (see SI, Fig. S7).

As mentioned before, anomalies seen for measurements along the a^* -axis are in general much weaker and less well-defined than for the c -axis. Furthermore, the evolution of anomalies in the thermal expansion and the static susceptibility along the a^* -axis is even more complex than for $B \parallel c$ (Fig. 5(c) and (d)). In zero-field, the anomaly at T^* is also visible (see Fig. 1, as well as SI, Fig. S10(d) and can be traced up to 0.4 T in $\partial\chi/\partial T$. Also, a jump in α_{a^*} evolving from T_{N1} can be followed to lower temperatures for increasing fields, corresponding to a jump in $\partial\chi/\partial T$. Above 0.6 T this jump splits into two jumps, uncovering an additional phase between the IC-2 and fiFM phases, while we only see one broad jump in α_{a^*} .

IV. DISCUSSION

From our detailed dilatometric and thermodynamic data we construct the phase diagrams for the c - and a^* -axes in Fig. 6. While the general features for $B \parallel c$ confirm previous results^{8,9,25}, our data evidence two phases in zero-field which were previously unknown: (1) Our isothermal magnetization data between 19 K and 22 K (SI, Fig. S7) clearly indicate that the IC-2 phase does not extend to zero field, but there is a separate pocket closed off by a phase boundary extending from the edge of the A(SkL) phase to $T_{N1} = 22.3$ K. We label

this new phase IC-3, since incommensurate spin structures were previously reported for this temperature regime⁸. (2) Furthermore, the phase boundary at T^* splits the IC-1 phase into IC-1 and IC-1' (Fig. 1(b) inset). The yet unreported phase diagram for $B \parallel a^*$ in general shows a similar behavior, with the critical fields of the IC-1' and IC-4 phases at lowest temperatures assuming higher values than IC-1' and the A phase for the c -axis. The IC-4 phase appearing for $B \parallel a^*$ (see Fig. 6b) reminds of the A(SkL) phase for $B \parallel c$, however, it was shown previously by angle-dependent resistivity measurements in the a^* - c -plane at 2 K that it does not connect to the A(SkL) phase.⁴² The magnetic structure of this phase needs to be clarified by diffraction studies. One major difference between the phase diagrams is seen for $B \parallel a^*$, where the IC-2 phase is not directly adjacent to the field-induced FM phase, but there is an additional phase (labelled B) in between (see Fig. 5(c) and (d)). The B phase is bordered by two jumps both in c_p as well as in $\partial\chi/\partial T$.

From the anomalies in the thermal expansion, specific heat and magnetization at the phase boundaries we calculated the uniaxial pressure and field dependence of the critical temperatures and critical fields, as well as the entropy changes at the phase boundaries for $B \parallel c$ -axis. Considering $T^*(B)$ marking a continuous phase transition, the associated jumps in specific heat (Δc_p), magnetic susceptibility ($\Delta(\partial M/\partial B)$), and thermal expansion coefficient ($\Delta\alpha$) are connected with the magnetic field and pressure dependencies of T^* by the Ehrenfest-type relations (see e.g. Ref. [43,44])

$$\left(\frac{\partial T^*}{\partial B_i}\right)\Big|_p = -T^* \frac{\Delta\left(\frac{\partial M_i}{\partial T}\right)\Big|_B}{\Delta c_{p,B}} \quad (4)$$

and

$$\left(\frac{\partial T^*}{\partial p_i}\right)\Big|_B = T^* V_m \frac{\Delta\alpha_i}{\Delta c_p}. \quad (5)$$

Using the molar volume $V_m = 7.06 \cdot 10^{-5} \text{ m}^3/\text{mol}$ (see Ref. [22]) as well as the anomaly values presented above and in Tab. S7 – for their extraction from the experimental data see the supplement, Fig. S10 – we obtain a moderate uniaxial pressure dependence of $\partial T^*/\partial p_c = -1.4(3) \text{ K/GPa}$. In a field of 0.2 T, the field dependence is very small and amounts to only $\partial T^*/\partial B_c = -37(13) \text{ mK/T}$. At 0.3 T, $\partial T^*/\partial B_c$ rises to $-0.28(18) \text{ K/T}$. These results demonstrate that the IC-1 phase is stabilized both under pressure and applied field at the expense of the IC-1' phase. Also, from these values we can calculate the expected jump in $\partial M/\partial B$ ($\Delta\chi$), at $T^*(B)$ via

$$\left(\frac{\partial T^*}{\partial B}\right)\Big|_p = -\frac{\Delta\left(\frac{\partial M}{\partial B}\right)\Big|_{p,T}}{\Delta\left(\frac{\partial M}{\partial T}\right)\Big|_{p,B}}. \quad (6)$$

At 0.2 T this yields $\Delta\chi = -2 \cdot 10^{-4} \mu_B / (\text{f.u. T})$, which is well below the resolution limit of our experiment, explaining why our isothermal magnetization studies do not show anomalies at T^* (see SI, Fig. S10). Note, that in an early report on Gd_2PdSi_3 by Mallik et al. the authors detected a jump in the effective local field $|B_{\text{eff}}|$ at 15 K by Mössbauer spectroscopy and attributed it to a lower ordering temperature of one of the two Gd sites in Gd_2PdSi_3 . This transition was not detected in any of the later reports on single crystalline samples, but our results presented in this work clearly confirm its presence.

The phase boundaries between the A(SkL), IC-2, and DP phases are of discontinuous nature, exhibiting jumps $\Delta(dL_i/L_i)$ in the length changes and ΔM in the magnetization (i.e., Δm in magnetic moment). Therefore, the Clapeyron equations⁴³

$$\left(\frac{\partial T_c}{\partial p_i}\right)\Big|_B = V_m \frac{\frac{\Delta L_i}{L_i}}{\Delta S} \quad (7)$$

$$\left(\frac{\partial T_c}{\partial B_i}\right)\Big|_p = -\frac{\Delta m_i}{\Delta S} = -\frac{\Delta(M_i \cdot V)}{\Delta S} \quad (8)$$

$$\left(\frac{\partial B_c}{\partial p_i}\right)\Big|_T = V_m \frac{\frac{\Delta L_i}{L_i}}{\Delta m_i} \quad (9)$$

apply for the pressure and field dependence of the respective critical temperatures T_c and critical fields B_c . Hence, the observed slopes $\partial T_c / \partial B$ (see Tab. S1–S4) and the jumps ΔM allow us to obtain the associated entropy changes ΔS .

For the transition from the incommensurate IC-1' phase to the skyrmion lattice A phase, a jump $\Delta M = 0.99(10) \mu_B / \text{Gd}$ accompanies the c -axis contraction of $\Delta dL_c / L_c = -10.8(1.1) \cdot 10^{-6}$ at 4.3 K. Applying the above-mentioned thermodynamic relations yields small entropy changes on the order of $\Delta S_{\text{calc}} = 125(13)$ mJ/mol K and a negative uniaxial pressure dependence of $\partial T_c / \partial p_i = -6.1(9)$ K/GPa. At higher temperatures these values decrease down to 110(11) mJ/mol K and $-1.5(2)$ K/GPa at 16 K (see Tab. S1). At the transition from the skyrmion lattice A phase to the IC-2 phase the c -axis also contracts, but these contractions are much smaller ($\Delta dL_c / L_c = -2.4(3) \cdot 10^{-6}$ at 4.3 K) while the jumps in magnetization again roughly correspond to one Bohr magneton per Gd ion ($\Delta M = 1.01(11) \mu_B / \text{Gd}$ at 4.3 K). Accordingly, this phase boundary shows much smaller

Transition	T (K)	B_c (T)	$\Delta(dL/L)$ (10^{-6})	Δm (μ_B/Gd)	$\partial B_c/\partial T$ (T/K)	ΔS (mJ/mol K)	$\partial T_c/\partial p_i$ (K/GPa)	$\partial B_c/\partial p_i$ (mT/GPa)
IC-1 \rightarrow A(SkL)	4.3 ± 0.1	0.49 ± 0.02	-10.8 ± 1.1	1.0 ± 0.1	-0.01	125 ± 13	-6.1 ± 0.9	-50 ± 50
A(SkL) \rightarrow IC-2	4.3 ± 0.1	1.04 ± 0.03	-2.4 ± 0.3	1.0 ± 0.1	-0.03	360 ± 40	-0.47 ± 0.07	-15 ± 2

Table I: Relevant quantities and anomaly sizes at the phase boundaries of the skyrmion lattice phase, at $T = 4.3$ K, and in magnetic fields $B \parallel c$ which have been either directly extracted from the experimental data or were obtained by using thermodynamic relations as given in the text.

pressure dependence, i.e., $\partial T_c/\partial p_i = -0.47(7)$ K/GPa at 4.3 K (see Tab. S2). At the same time, the steeper slope of the phase boundary $B_c(T)$ implies larger changes in entropy of 360(40) mJ/mol K at 4.3 K which increases to almost 600(60) mJ/mol K at 16 K. We note that the analysis of anomalies from temperature instead of field sweeps confirms these values (Tab. S3). Looking at higher fields, the slope of the phase boundary from IC-2 to the depinned phase (DP) is very small, changing from a small negative slope below 6 K to a small positive slope above. Considering the measured anomalies $\Delta M = 0.08(4)\mu_B/\text{Gd}$ at 4.3 K, this yields negligible associated entropy changes (Tab. S4). In contrast, there are pronounced lattice effects ($\Delta dL_c/L_c = -17(2) \cdot 10^{-6}$ at 1.77 K) yielding a very large pressure dependence for the phase boundary IC-2 \rightarrow DP.

The results of the thermodynamic analyses are shown in table I as well in tables S1 to S4 in the supplement. In particular, our analysis evidences pronounced negative uniaxial pressure dependencies for all three phase transitions between IC-1/IC-1', A(SkL), IC-2 and DP at low temperatures. This implies that the IC-1'/IC-1, A(SkL) and IC-2 phases are all destabilized by pressure along the c -axis with respect to the higher temperature phases, i.e., the field-induced FM phase – and the paramagnetic phase at low fields – is stabilized.

In particular, our data for $B \parallel c$ provide further information on the skyrmion phase. Both the onset of the SkL phase from incommensurate magnetic order IC-1/IC-1' and its transition into the incommensurate IC-2 phase are discontinuous in nature. In both cases, transitions are associated with the increase of magnetization by about $1 \mu_B/\text{Gd}$. Rather flat phase boundaries in the magnetic phase diagram are indicative of comparably small entropy changes. Our quantitative analysis evidences that the evolution of the SkL phase,

depending on the temperature, yields an entropy gain of $\Delta S \approx 100 - 150$ mJ/(mol K) while the entropy jumps at the transition out of the skyrmion phase by 300-600 mJ/(mol K). These values are by far larger than for the chiral magnet MnSi where latent heat at the phase boundaries only amount to a few mJ/(mol K).⁴⁵ Uniaxial pressure along the c -axis significantly enhances the SkL phase as seen by the uniaxial pressure dependencies of the transition temperatures. Specifically, at 4 K there is a rapid decrease of the IC-1/IC-1' \rightarrow A(SkL) transition temperature $\partial T_{\text{in}}/\partial p_c \approx -6$ K/GPa, leading to an expansion of the A(SkL) phase towards lower temperatures under pressure. At the same time the temperature of the A(SkL) \rightarrow IC-2 transition, i.e. exiting the SkL phase towards higher temperatures, changes by only $\partial T_{\text{out}}/\partial p_c \approx -0.5$ K/GPa (see tables I and II). Enhancement of skyrmion lattice phases under pressure is also observed in other materials. In the insulating skyrmion system Cu_2OSeO_3 , Levatić et al. report a dramatic enhancement of the skyrmion pocket under pressure by about 8 K at 0.6 GPa.⁴⁶ While in Gd_2PdSi_3 the SkL phase appears at lower temperatures, our results ($\partial T_{\text{in}}/\partial p_c - \partial T_{\text{out}}/\partial p_c$) imply about half of this effect. We also note similar findings to the ones reported at hand in the chiral magnet MnSi^{47,48} where uniaxial pressure along [001] yields a rapid decrease of the onset temperature of the skyrmion phase while the high temperature phase boundary shows a much smaller pressure dependence.⁴⁹ Recent theoretical studies by Hayami et al. investigated the influence of single-ion anisotropy on the formation and stability of the skyrmion lattice phase. They show that easy-axis anisotropies stabilize magnetic-field-induced skyrmion crystals in frustrated magnets⁵⁰ and easy-axis (easy-plane) anisotropy substantially increases (decreases) the stable field-range for a Skyrmion lattice. These findings suggest, that the pressure dependencies stabilizing the skyrmion lattice phase in Gd_2PdSi_3 may originate from small distortions in the local environment of Gd leading to an increase of the weak magnetic anisotropy of the Gd moments.

The transition from the depinned phase to the field-induced ferromagnetic phase is of a continuous type. It exhibits a jump in the magnetostriction coefficient $\Delta\lambda = -4.7(5) \cdot 10^{-5}/T$ (at 1.77 K) and in the derivative of the magnetization $\Delta\partial M/\partial B = -0.159(16)\mu_B/(T \text{ Gd})$ ($T = 1.9$ K). Using an Ehrenfest relation, the uniaxial pressure dependence of the critical field can be expressed as $dB_c/dp_i = \Delta\lambda/\Delta(dM/dB)$, which yields $dB_c/dp_c = 1.9(5)$ T/GPa at 1.77 K, i.e. the depinned phase is stabilized under uniaxial pressure p_c . Similarly, using the anomaly values listed in Tab. S5, we find uniaxial pressure dependencies of the critical

field between $-0.65(16)$ T/GPa (10 K) and $-0.50(8)$ T/GPa (14 K) at the continuous transition IC-2 to fFM.

While Gd_2PdSi_3 shows only moderate frustration, magnetic entropy and length changes are observed up to about $2.7 T_{\text{N}1}$ (60 K), thereby implying the evolution of short range magnetic order in this temperature regime. Effects of fluctuations above T_{N} in Gd_2PdSi_3 were observed before in resistivity measurements. Measurements on polycrystalline samples show a well-defined minimum around 45 K⁵¹ which was also confirmed in single crystals¹⁷. A theoretical explanation of this behavior based on the RKKY-interaction in combination with frustration was given by Wang et al.⁵². Grüneisen scaling suggests that these precursor fluctuations are of the IC-1/IC-3 type. Both ordering phenomena are driven by the same dominating energy scale which differs from the one driving IC-1'. As expected for a Gd^{3+} -system, magnetoelastic coupling is moderate. It is, hence, somehow surprising that magnetostriction is large at high temperatures and displays pronounced effects up to 200 K. In addition, despite linear field dependence of the magnetization, magnetostriction does not follow a B^2 -law below 200 K (see Fig. S6) as would be expected from the relation $dL_i/L_i = -1/2V \partial\chi_i/\partial p_i B^2$ in the paramagnetic regime [53]. Tentatively, magnetostriction above 100 K implies negative uniaxial pressure dependence, $\partial\chi/\partial p_c < 0$, of the magnetic susceptibility while $\partial\chi/\partial p_{a^*} > 0$. This observation suggests that antiferromagnetic exchange interactions are strengthened by uniaxial pressure along the c -axis and weakened upon application of $p \parallel a^*$. Notably, however, the long-range magnetic ordering temperatures do not follow this trend as $\partial T_{\text{N}}/\partial p_c < 0$ which further highlights the complex nature of magnetism in Gd_2PdSi_3 .

V. CONCLUSIONS

For the first time, high-resolution dilatometry was used to study the interplay between magnetism and the lattice of single crystalline Gd_2PdSi_3 . Strong magnetoelastic coupling and field effects up to high temperatures are found. Pronounced anomalies in the thermal expansion, magnetostriction and magnetization allow us to obtain the magnetic phase diagram. This yields in particular several novel phases for $B \parallel c$ while the B vs. T phase diagram for $B \parallel a^*$ has not yet been reported at all in the literature. Grüneisen analysis shows the onset of magnetic contributions well above $T_{\text{N}1}$, and the pressure dependencies

of ordering phenomena are obtained. In particular, we find that uniaxial pressure strongly enhances the skyrmion lattice phase.

Acknowledgements

We thank I. Mazilu and Y. Xu for support in the crystal growth. We acknowledge financial support by BMBF via the project SpinFun (13XP5088) and by Deutsche Forschungsgemeinschaft (DFG) under Germany's Excellence Strategy EXC2181/1-390900948 (the Heidelberg STRUCTURES Excellence Cluster), through project KL 1824/13-1, and within the SFB 463.

* Electronic address: sven.spachmann@kip.uni-heidelberg.de

- ¹ R.-D. Hoffmann and R. Pöttgen, *Zeitschrift für Kristallographie - Crystalline Materials* **216**, 127 (2001), URL <https://doi.org/10.1524/zkri.216.3.127.20327>.
- ² Z.-Y. Pan, C.-D. Cao, X.-J. Bai, R.-B. Song, J.-B. Zheng, and L.-B. Duan, *Chinese Physics B* **22**, 056102 (2013), URL <https://doi.org/10.1088/1674-1056/22/5/056102>.
- ³ S. Majumdar and E. V. Sampathkumaran, *Physical Review B* **63**, 172407 (2001), URL <https://link.aps.org/doi/10.1103/PhysRevB.63.172407>.
- ⁴ S. Majumdar, E. V. Sampathkumaran, P. L. Paulose, H. Bitterlich, W. Löser, and G. Behr, *Physical Review B* **62**, 14207 (2000).
- ⁵ S. Majumdar, H. Bitterlich, G. Behr, W. Löser, P. L. Paulose, and E. V. Sampathkumaran, *Physical Review B* **64**, 012418 (2001), URL <https://link.aps.org/doi/10.1103/PhysRevB.64.012418>.
- ⁶ P. L. Paulose, E. V. Sampathkumaran, H. Bitterlich, G. Behr, and W. Löser, *Physical Review B* **67**, 212401 (2003), URL <https://link.aps.org/doi/10.1103/PhysRevB.67.212401>.
- ⁷ C. D. Cao, R. Klingeler, H. Vinzelberg, N. Leps, W. Löser, G. Behr, F. Muranyi, V. Kataev, and B. Büchner, *Physical Review B* **82**, 134446 (2010), URL <https://link.aps.org/doi/10.1103/PhysRevB.82.134446>.
- ⁸ T. Kurumaji, T. Nakajima, M. Hirschberger, A. Kikkawa, Y. Yamasaki, H. Sagayama, H. Nakao, Y. Taguchi, T. Arima, and Y. Tokura, *Science* **365**, 914 (2019), ISSN 0036-8075, URL <https://doi.org/10.1126/science.1258100>.

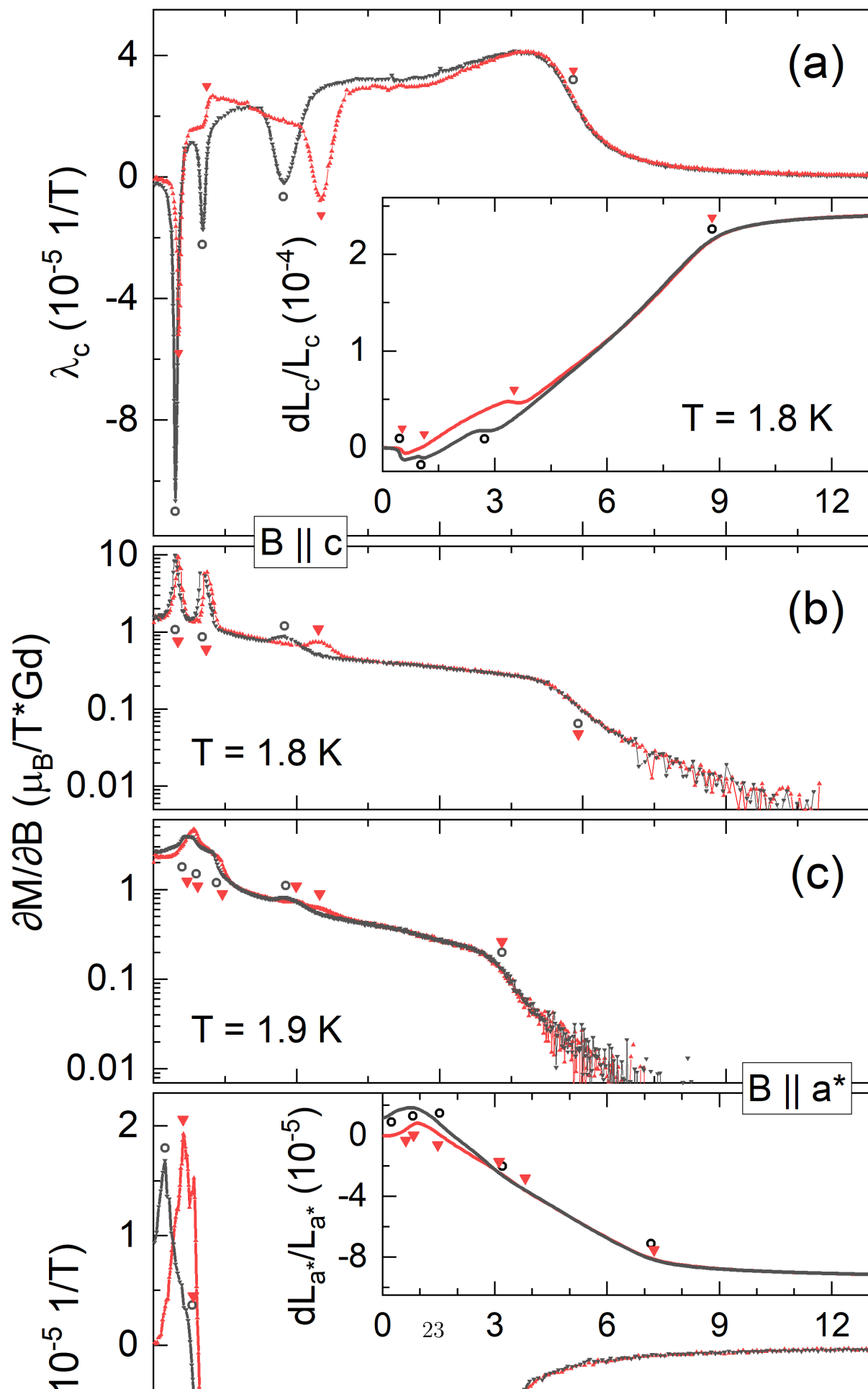
[//science.sciencemag.org/content/365/6456/914](https://science.sciencemag.org/content/365/6456/914).

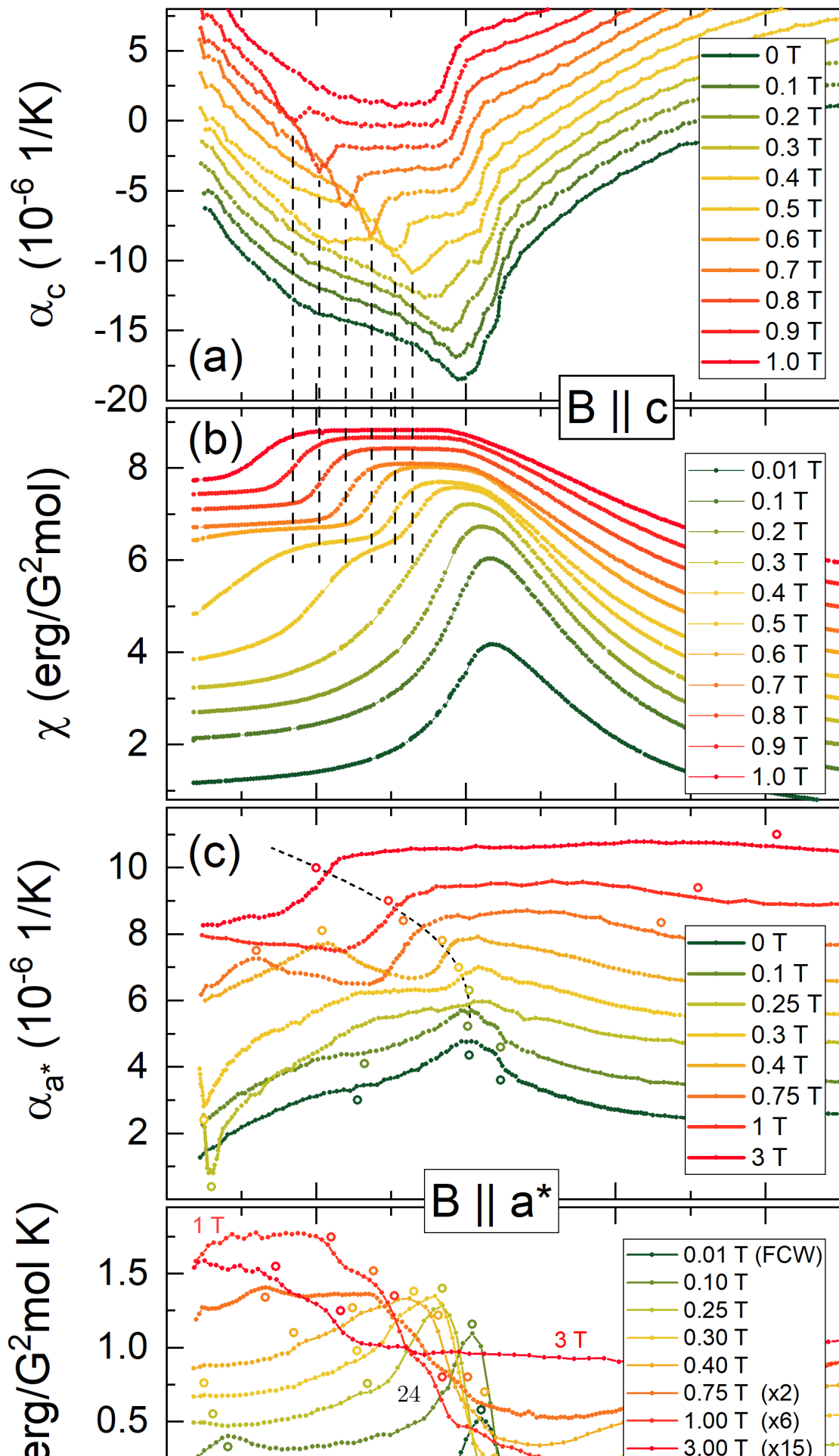
- ⁹ M. Hirschberger, T. Nakajima, M. Kriener, T. Kurumaji, L. Spitz, S. Gao, A. Kikkawa, Y. Yamasaki, H. Sagayama, H. Nakao, et al., *Physical Review B* **101**, 220401(R) (2020), ISSN 24699969, 2004.05385, URL <https://doi.org/10.1103/PhysRevB.101.220401>.
- ¹⁰ S. Majumdar, M. Mahesh Kumar, R. Mallik, and E. Sampathkumaran, *Solid State Communications* **110**, 509 (1999), ISSN 0038-1098, URL <https://www.sciencedirect.com/science/article/pii/S0038109899001040>.
- ¹¹ S. R. Saha, H. Sugawara, T. D. Matsuda, Y. Aoki, H. Sato, and E. V. Sampathkumaran, *Physical Review B* **62**, 425 (2000), URL <https://link.aps.org/doi/10.1103/PhysRevB.62.425>.
- ¹² S. Majumdar, E. V. Sampathkumaran, S. Berger, M. Della Mea, H. Michor, E. Bauer, M. Brando, J. Hemberger, and A. Loidl, *Solid State Communications* **121**, 665 (2002), ISSN 0038-1098, URL <https://www.sciencedirect.com/science/article/pii/S0038109802000534>.
- ¹³ D. Kaczorowski and H. Noel, *Journal of Physics: Condensed Matter* **5**, 9185 (1993), URL <https://doi.org/10.1088/0953-8984/5/49/020>.
- ¹⁴ C. Tien, L. Luo, and J. S. Hwang, *Physical Review B* **56**, 11710 (1997), URL <https://link.aps.org/doi/10.1103/PhysRevB.56.11710>.
- ¹⁵ D. X. Li, A. Dönni, Y. Kimura, Y. Shiokawa, Y. Homma, Y. Haga, E. Yamamoto, T. Honma, and Y. Onuki, *Journal of Physics: Condensed Matter* **11**, 8263 (1999), URL <https://doi.org/10.1088/0953-8984/11/42/307>.
- ¹⁶ D. X. Li, S. Nimori, Y. Shiokawa, Y. Haga, E. Yamamoto, and Y. Onuki, *Physical Review B* **68**, 012413 (2003), URL <https://link.aps.org/doi/10.1103/PhysRevB.68.012413>.
- ¹⁷ S. R. Saha, H. Sugawara, T. D. Matsuda, H. Sato, R. Mallik, and E. V. Sampathkumaran, *Physical Review B* **60**, 12162 (1999), URL <https://link.aps.org/doi/10.1103/PhysRevB.60.12162>.
- ¹⁸ M. Hirschberger, L. Spitz, T. Nomoto, T. Kurumaji, S. Gao, J. Masell, T. Nakajima, A. Kikkawa, Y. Yamasaki, H. Sagayama, et al., *Physical Review Letters* **125**, 076602 (2020), ISSN 10797114, 1910.06027, URL <https://doi.org/10.1103/PhysRevLett.125.076602>.
- ¹⁹ A. Szytuła, M. Hofmann, B. Penc, M. Ślaski, S. Majumdar, E. V. Sampathkumaran, and A. Zygmunt, *Journal of Magnetism and Magnetic Materials* **202**, 365 (1999), ISSN 0304-8853,

- URL <https://www.sciencedirect.com/science/article/pii/S0304885399004102>.
- ²⁰ F. Tang, M. Frontzek, J. Dshemuchadse, T. Leisegang, M. Zschornak, R. Mietrach, J.-U. Hoffmann, W. Löser, S. Gemming, D. C. Meyer, et al., *Physical Review B* **84**, 104105 (2011), URL <https://link.aps.org/doi/10.1103/PhysRevB.84.104105>.
- ²¹ F. Tang, P. Link, M. Frontzek, A. Schneidewind, W. Löser, and M. Loewenhaupt, *Journal of Physics: Conference Series* **251**, 012004 (2010), URL <https://doi.org/10.1088/1742-6596/251/1/012004>.
- ²² M. Frontzek, Ph.D. Thesis, Technische Universität Dresden (2009), URL <https://nbn-resolving.org/urn:nbn:de:bsz:14-qucosa-24779>.
- ²³ M. Smidman, C. Ritter, D. T. Adroja, S. Rayaprol, T. Basu, E. V. Sampathkumaran, and A. D. Hillier, *Physical Review B* **100**, 134423 (2019), URL <https://link.aps.org/doi/10.1103/PhysRevB.100.134423>.
- ²⁴ K. Mukherjee, T. Basu, K. K. Iyer, and E. V. Sampathkumaran, *Physical Review B* **84**, 184415 (2011), URL <https://link.aps.org/doi/10.1103/PhysRevB.84.184415>.
- ²⁵ H. Zhang, Q. Huang, L. Hao, J. Yang, K. Noordhoek, S. Pandey, H. Zhou, and J. Liu, arXiv (2020), ISSN 23318422, 2004.09664.
- ²⁶ Here, $\Delta a = a(300\text{ K}) - a(2\text{ K})$ and Δc analogously.
- ²⁷ I. Mazilu, Ph.D. Thesis, Technische Universität Darmstadt (2006).
- ²⁸ Y. Xu, M. Frontzek, I. Mazilu, W. Löser, G. Behr, B. Büchner, and L. Liu, *Journal of Crystal Growth* **318**, 942 (2011), ISSN 00220248.
- ²⁹ D. S. Inosov, D. V. Evtushinsky, A. Koitzsch, V. B. Zabolotnyy, S. V. Borisenko, A. A. Kordyuk, M. Frontzek, M. Loewenhaupt, W. Löser, I. Mazilu, et al., *Physical Review Letters* **102**, 046401 (2009), ISSN 0031-9007, 0808.2898, URL <https://link.aps.org/doi/10.1103/PhysRevLett.102.046401>.
- ³⁰ R. Küchler, T. Bauer, M. Brando, and F. Steglich, *Review of Scientific Instruments* **83**, 095102 (2012), <https://doi.org/10.1063/1.4748864>, URL <https://doi.org/10.1063/1.4748864>.
- ³¹ J. Werner, W. Hergett, M. Gertig, J. Park, C. Koo, and R. Klingeler, *Physical Review B* **95**, 214414 (2017), URL <https://link.aps.org/doi/10.1103/PhysRevB.95.214414>.
- ³² C. Cao, C. G. F. Blum, T. Ritschel, S. Rodan, L. Giebeler, D. Bombor, S. Wurmehl, and W. Löser, *CrystEngComm* **15**, 9052 (2013), ISSN 14668033.
- ³³ A. Tari, *The Specific Heat of Matter at Low Temperatures* (Published by

- Imperial College Press and distributed by World Scientific Publishing Co., 2003), <https://www.worldscientific.com/doi/pdf/10.1142/p254>, URL <https://www.worldscientific.com/doi/abs/10.1142/p254>.
- ³⁴ P. Gegenwart, Rep. Prog. Phys. **79**, 114502 (2016), URL <https://iopscience.iop.org/article/10.1088/0034-4885/79/11/114502>.
- ³⁵ R. Klingeler, J. Geck, S. Arumugam, N. Tristan, P. Reutler, B. Büchner, L. Pinsard-Gaudart, and A. Revcolevschi, Phys. Rev. B **73**, 214432 (2006), URL <https://link.aps.org/doi/10.1103/PhysRevB.73.214432>.
- ³⁶ The T -scale for $\alpha_{c,\text{mag}}$ was shifted by +0.4 K to match the specific heat anomaly.
- ³⁷ V. M. Kalita, A. F. Lozenko, and S. M. Ryabchenko, Low Temperature Physics **26**, 489 (2000), <https://doi.org/10.1063/1.1306404>, URL <https://doi.org/10.1063/1.1306404>.
- ³⁸ V. M. Kalita, A. F. Lozenko, and P. A. Trotsenko, Low Temperature Physics **28**, 263 (2002), <https://doi.org/10.1063/1.1477360>, URL <https://doi.org/10.1063/1.1477360>.
- ³⁹ K. Dey, S. Sauerland, B. Ouladdiaf, K. Beauvois, H. Wadepohl, and R. Klingeler, *Magnetostructural coupling in ilmenite-type NiTiO₃: a combined diffraction and dilatometry study* (2021), arxiv:2102.09417.
- ⁴⁰ For the field-cooled warming protocol, the sample is cooled in the applied field to lowest temperatures and measured during the subsequent warming process.
- ⁴¹ Magnetization measurements have been performed following the zero-field cooling (ZFC) protocol unless stated otherwise, i.e., the sample was cooled to lowest temperatures before the field was applied and the data were recorded during warming.
- ⁴² M. Hirschberger, T. Nakajima, S. Gao, L. Peng, A. Kikkawa, T. Kurumaji, M. Kriener, Y. Yamasaki, H. Sagayama, H. Nakao, et al., Nature Communications **10**, 1 (2019), ISSN 20411723, URL <http://dx.doi.org/10.1038/s41467-019-13675-4>.
- ⁴³ T. H. K. Barron and G. K. White, *Heat Capacity and Thermal Expansion at Low Temperatures*, The International Cryogenic Monograph Series (Kluwer Academic / Plenum Publishers, 1999).
- ⁴⁴ R. Klingeler, B. Büchner, S.-W. Cheong, and M. Hücker, Physical Review B **72**, 104424 (2005), URL <https://link.aps.org/doi/10.1103/PhysRevB.72.104424>.
- ⁴⁵ A. Bauer, M. Garst, and C. Pfleiderer, Physical Review Letters **110**, 177207 (2013), URL <https://link.aps.org/doi/10.1103/PhysRevLett.110.177207>.
- ⁴⁶ I. Levatić, P. Popčević, V. Šurija, A. Kruchkov, H. Berger, A. Magrez, J. S. White,

- H. M. Rønnow, and I. Živković, Scientific reports **6**, 21347 (2016), ISSN 2045-2322, URL <https://pubmed.ncbi.nlm.nih.gov/26892190><https://www.ncbi.nlm.nih.gov/pmc/articles/PMC4759555/>.
- ⁴⁷ A. Chacon, A. Bauer, T. Adams, F. Rucker, G. Brandl, R. Georgii, M. Garst, and C. Pfeiferer, Physical Review Letters **115**, 267202 (2015), URL <https://link.aps.org/doi/10.1103/PhysRevLett.115.267202>.
- ⁴⁸ Y. Nii, T. Nakajima, A. Kikkawa, Y. Yamasaki, K. Ohishi, J. Suzuki, Y. Taguchi, T. Arima, Y. Tokura, and Y. Iwasa, Nature Communications **6**, 8539 (2015), ISSN 2041-1723, URL <https://doi.org/10.1038/ncomms9539>.
- ⁴⁹ For MnSi, this also holds for pressure along [111] and [110]. From our data, only uniaxial pressure effects $p \parallel c$ are accessible so that a comparison for the other directions cannot be made.
- ⁵⁰ S. Hayami, S.-Z. Lin, and C. D. Batista, Physical Review B **93**, 184413 (2016), URL <https://link.aps.org/doi/10.1103/PhysRevB.93.184413>.
- ⁵¹ R. Mallik, E. V. Sampathkumaran, M. Strecker, and G. Wortmann, Europhysics Letters **41**, 315 (1998), ISSN 02955075.
- ⁵² Z. Wang, K. Barros, G.-W. Chern, D. L. Maslov, and C. D. Batista, Physical Review Letters **117**, 206601 (2016), URL <https://link.aps.org/doi/10.1103/PhysRevLett.117.206601>.
- ⁵³ N. Johannsen, A. Vasiliev, A. Oosawa, H. Tanaka, and T. Lorenz, Physical Review Letters **95**, 017205 (2005), URL <https://link.aps.org/doi/10.1103/PhysRevLett.95.017205>.





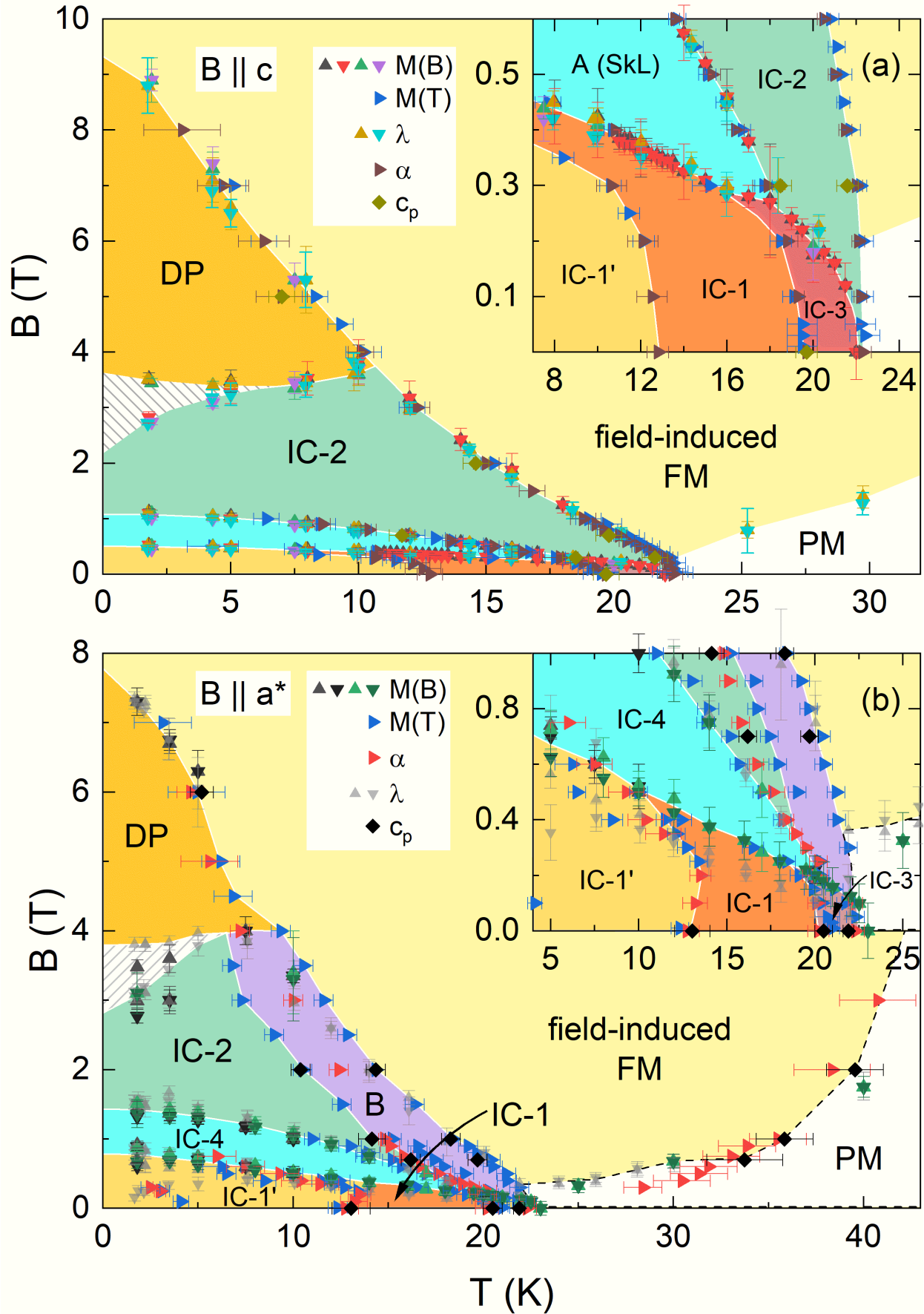


Figure 6: Phase diagrams for (a) $B \parallel c$ and (b) $B \parallel a^*$ constructed from different experimental techniques as indicated in the legends. The shaded areas show two strong hysteresis regimes. The

Supplementary Material:
Magnetoelastic Coupling and Phases in the Skyrmion
Lattice Magnet Gd_2PdSi_3 Discovered by High-
resolution Dilatometry

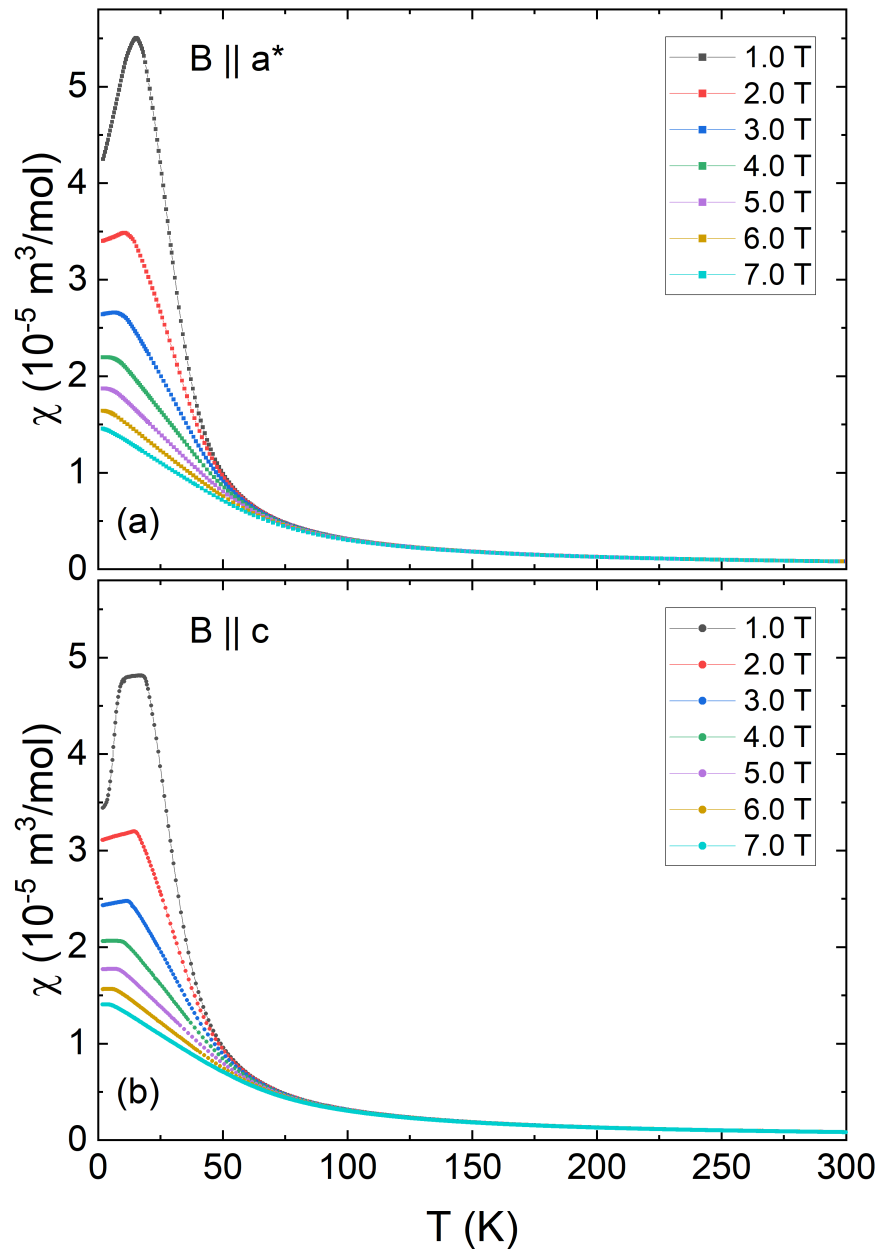


Figure S1: Static magnetic susceptibility $\chi = M/B$ for (a) $B \parallel a^*$ and (b) $B \parallel c$ (b).

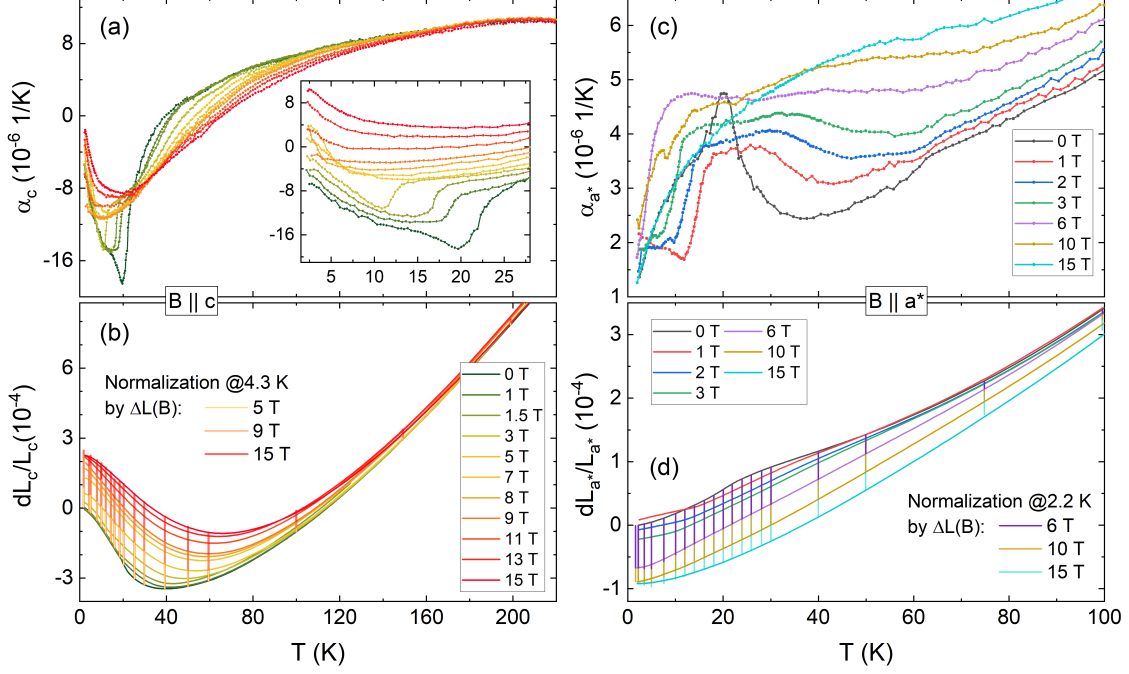


Figure S2: (a-b) Thermal expansion measurements up to 220 K for $B \parallel c$ in magnetic fields up to 15 T. (a) Thermal expansion coefficient α_c . The inset shows the magnified low temperature region with an offset of $1.2 \cdot 10^{-6} \text{ 1/K}$. (b) Relative length changes $dL_c(T)/L_c$. Vertical lines mark the changes $\Delta L(B)/L$ derived from magnetostriction measurements. The data at different fields are normalized by these changes at 4.3 K. (c-d) Thermal expansion measurements up to 100 K for $B \parallel a^*$ in magnetic fields up to 15 T. (c) Thermal expansion coefficient α_{a^*} offset by $2 \cdot 10^{-7} \text{ 1/K}$. (d) Relative length changes $dL_{a^*}(T)/L_{a^*}$. Vertical lines again mark the changes $\Delta L(B)/L$ taken from magnetostriction measurements. The data at different fields are offset and normalized by these changes at 2.2 K w.r.t. the zero-field data.

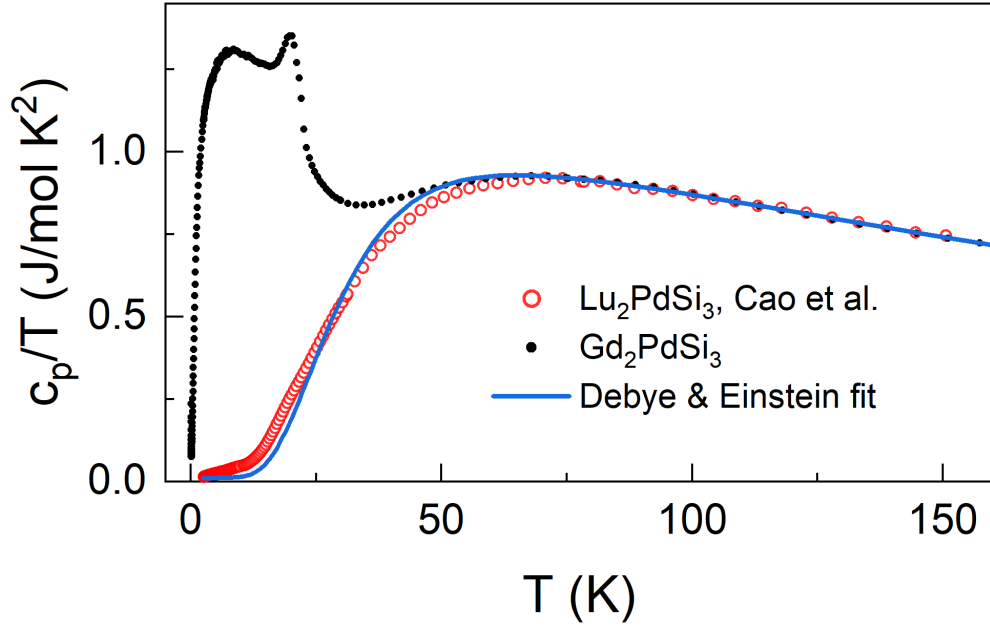


Figure S3: Comparison of the scaled Lu₂PdSi₃ specific heat c_p/T measured by Cao et al.³² (red empty circles) with the Debye and Einstein fit (blue line). Note that the Lu₂PdSi₃ data was interpolated and therefore contains more data points than the published data.

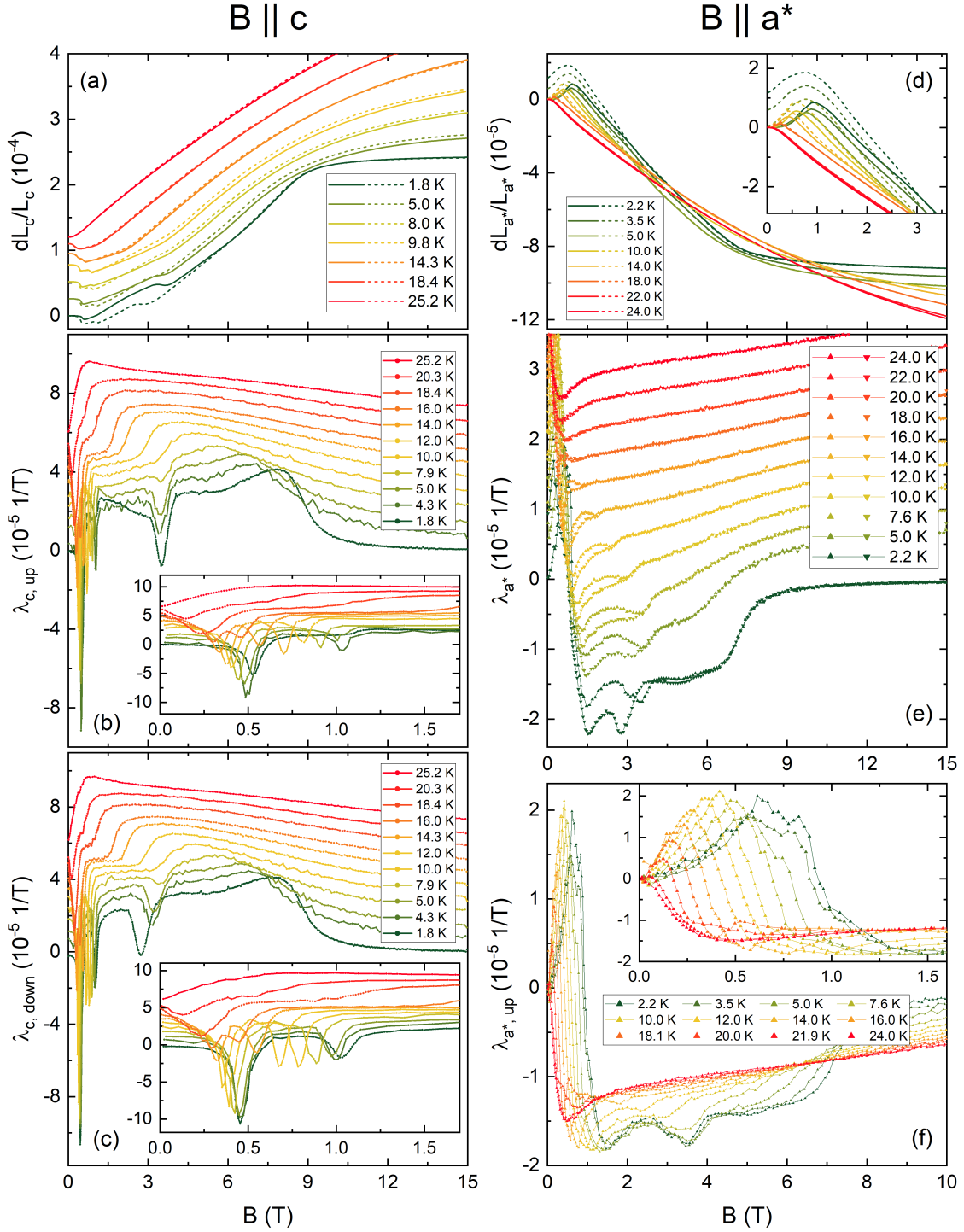


Figure S4: Magnetostriction measurements at temperatures from 1.7 K to 25 K for $B \parallel c$ (a-c) and $B \parallel a^*$ (d-f): The relative length change $dL(B)/L$ (a, d) and magnetostriction coefficient λ_i (b, c, e, f) are shown. Solid lines in (a, d) represent up-sweeps, dashed lines down-sweeps. Triangles pointing upwards in (d) mark up-sweeps, triangles pointing downwards mark down-sweeps. Data in (a-c, insets also) and (e) are shifted vertically for better visibility by: (a) different amounts, (b, c) $6 \cdot 10^{-6} \text{ 1/T}$, (e) $3.7 \cdot 10^{-6} \text{ 1/T}$ (3.5 K data is omitted). Insets show magnifications of the low field regions.

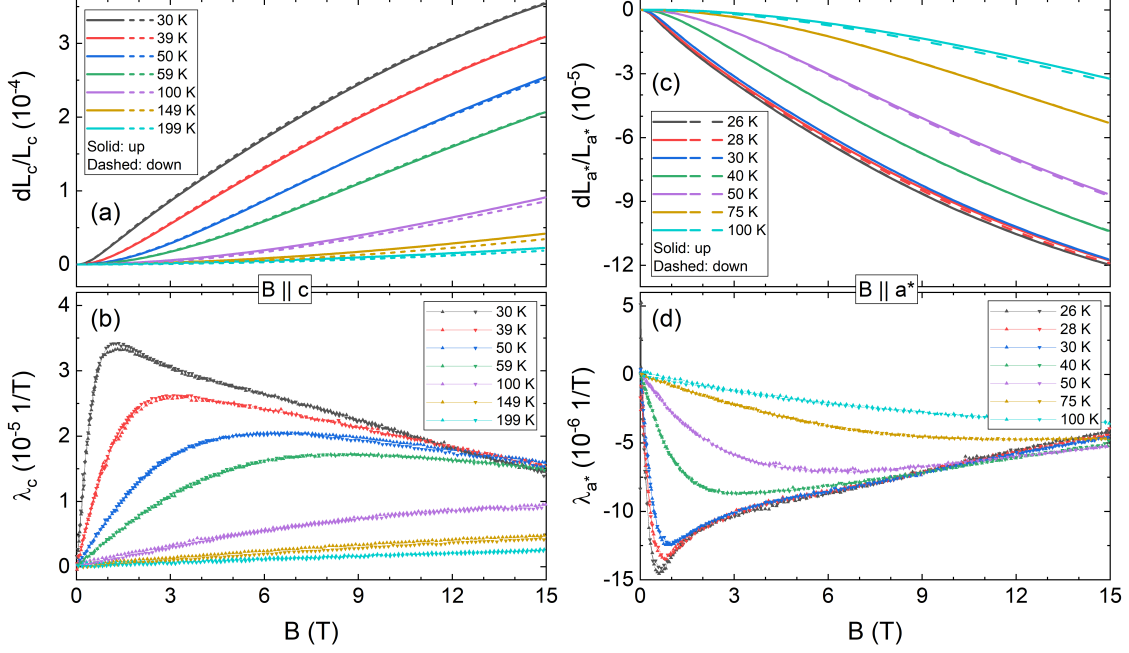


Figure S5: Magnetostriction measurements at temperatures above T_{N1} for $B \parallel c$ (a-b) and $B \parallel a^*$ (c-d): The relative length change $dL(B)/L$ (a, c) and magnetostriction coefficient λ_i (b, d) are shown. Solid lines in (a, c) represent up-sweeps, dashed lines down-sweeps. Triangles pointing upwards in (b, d) are up-sweeps, triangles pointing downwards mark down-sweeps.

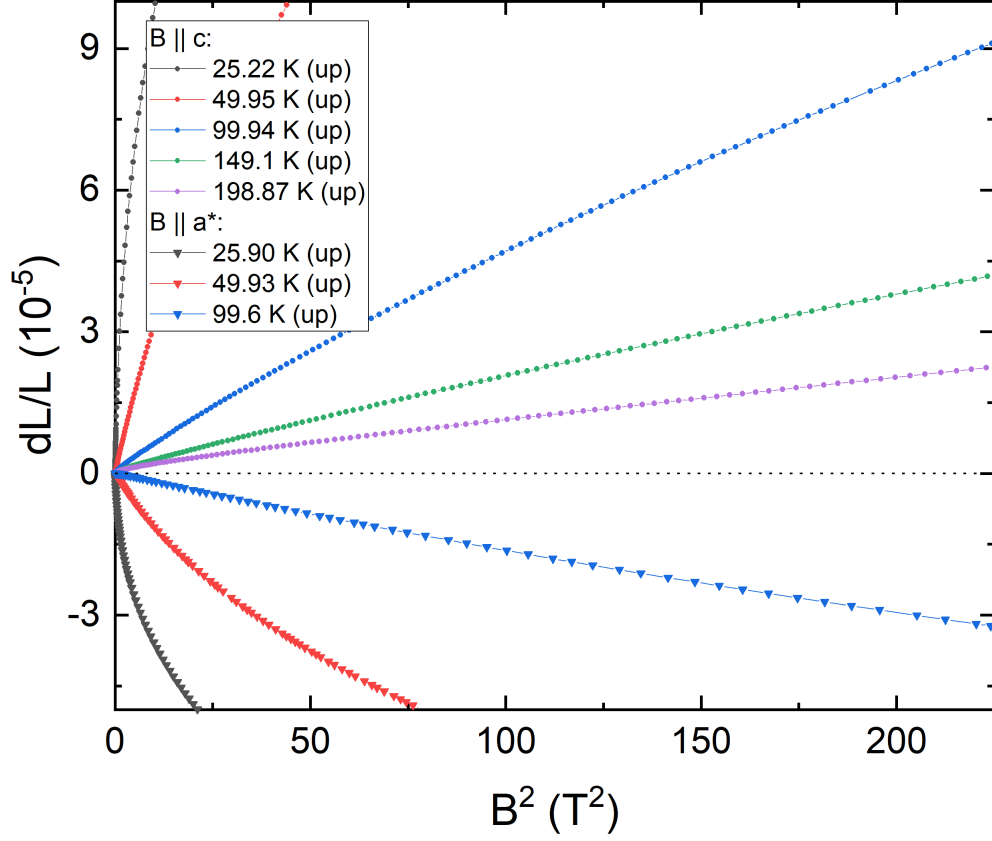


Figure S6: Relative length changes dL/L plotted vs. B^2 . The uniaxial pressure dependence of the susceptibility is related to the magnetostriction by the Maxwell relation $\partial(dL/L)/\partial B = -\partial M/\partial p$. For a paramagnetic material with $M = \chi B$ we thus have $dL/L = -\frac{1}{2}\partial\chi/\partial p B^2$, i.e. $\partial\chi/\partial p$ is proportional to the slope in the above plot.

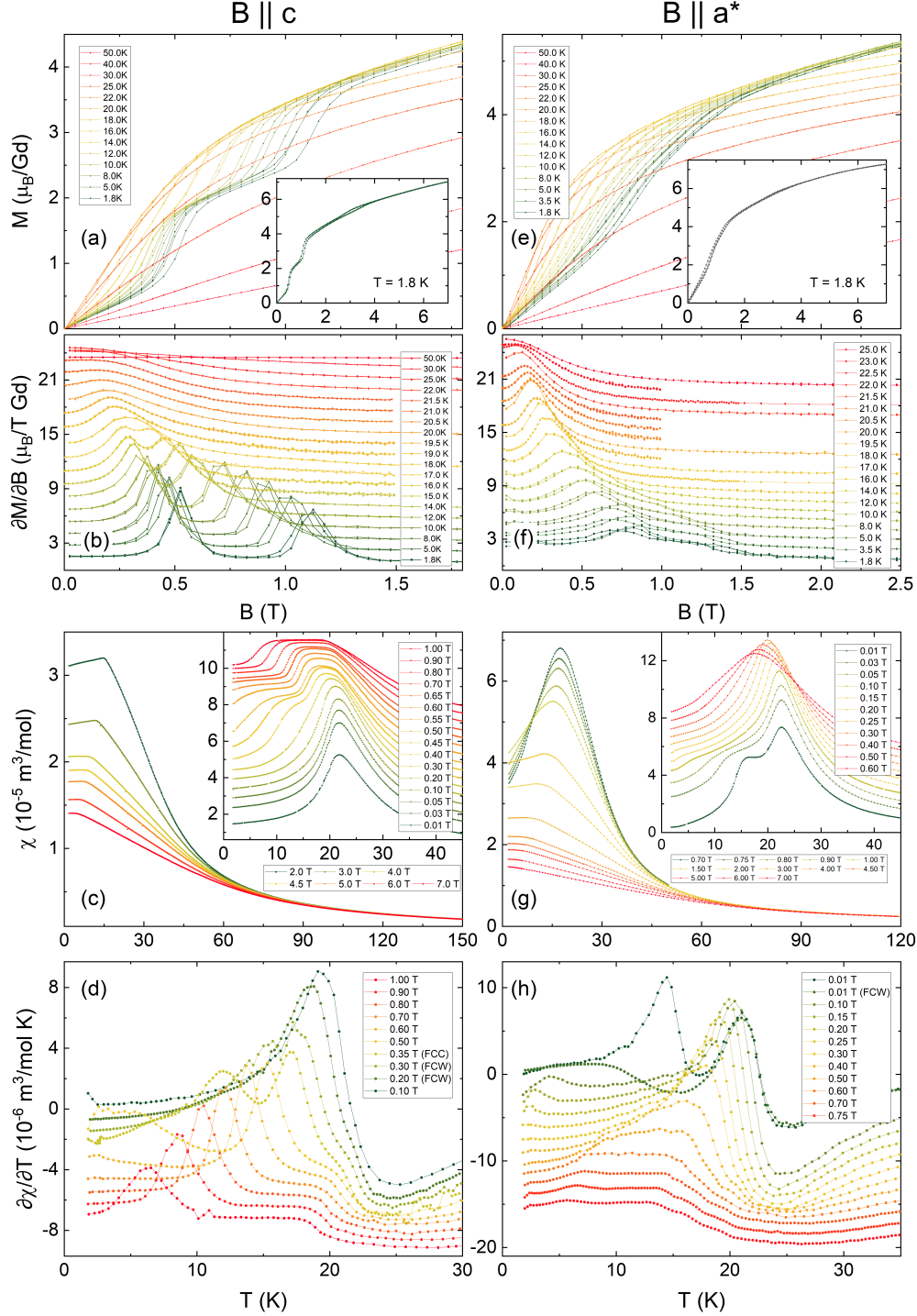


Figure S7: Measurements of the isothermal magnetization as well as the static magnetic susceptibility $\chi(T)$ and their derivatives for $B \parallel c$ (a-d) and $B \parallel a^*$ (e-h). $\chi(T)$ measurements were performed in a zero-field cooled manner unless stated otherwise (FCW: field-cooled warming, FCC: field-cooled cooling). Data are offset for better visibility by (b) $1.2 \mu_B/(T \text{ Gd})$, (c, inset) $4.5 \cdot 10^{-6} \text{ m}^3/\text{mol}$, (d) $-8 \cdot 10^{-7} \text{ m}^3/(\text{mol K})$, (f) $1.1 \mu_B/(T \text{ Gd})$, (g, inset) $5 \cdot 10^{-6} \text{ m}^3/\text{mol}$, and (h) $-1.4 \cdot 10^{-6} \text{ m}^3/(\text{mol K})$ starting with the data for $B = 0.10 \text{ T}$.

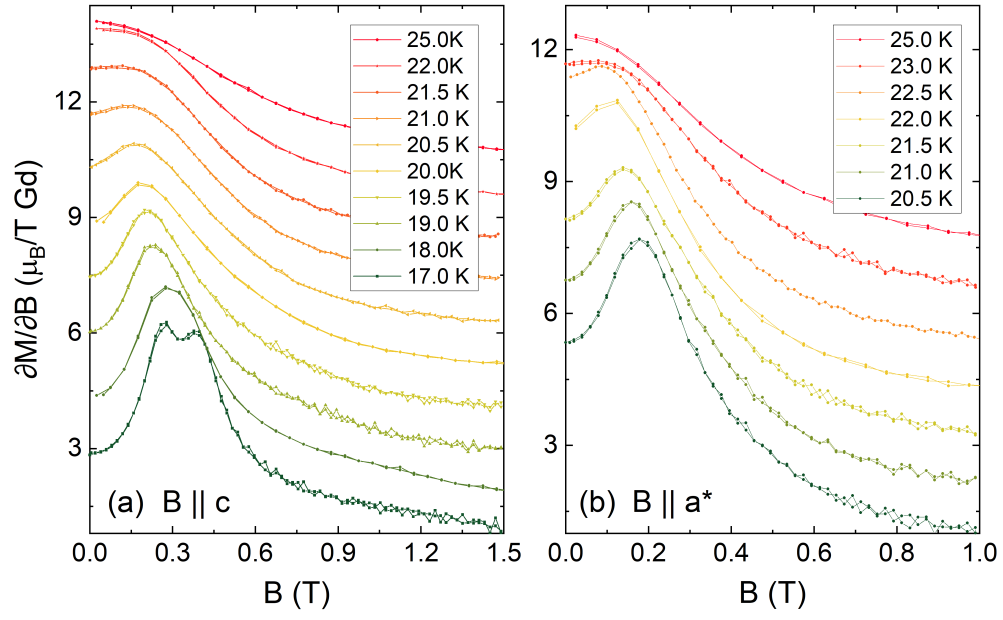


Figure S8: Close-up of the measurements of the magnetic susceptibility $\partial M/\partial B$ for $B \parallel c$ (a) and $B \parallel a^*$ (b) in the temperature regime of the IC-3 \rightarrow IC-2 transition.

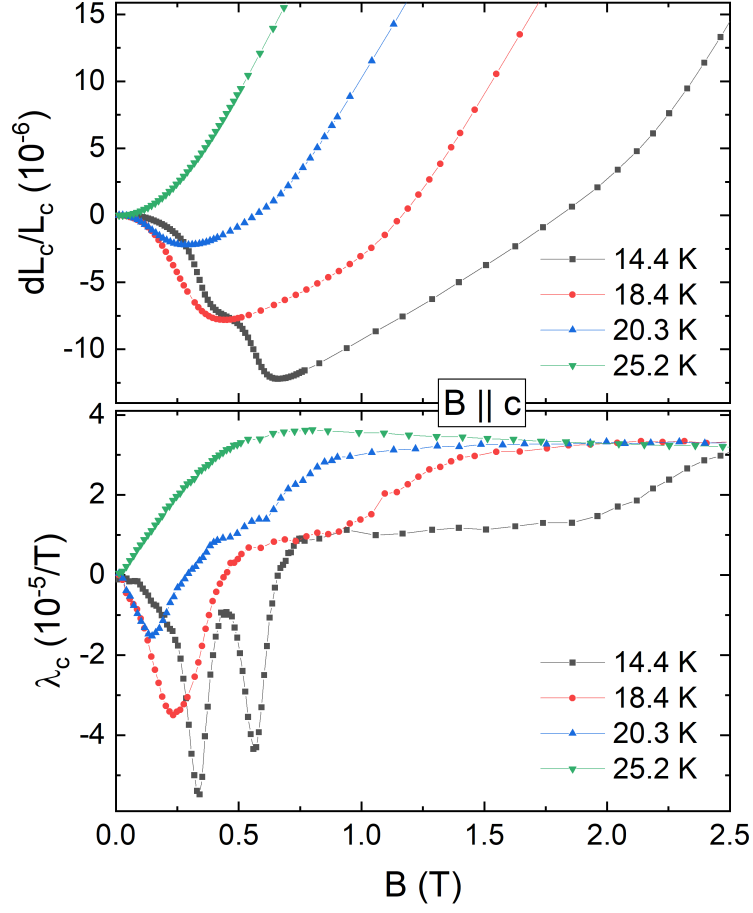


Figure S9: (a) Relative length changes dL_c/L_c and (b) magnetostriction coefficient λ_c in the low-field regime at temperatures below and above T_{N1} and T_{N2} for $B \parallel c$. Only up-sweeps are shown.

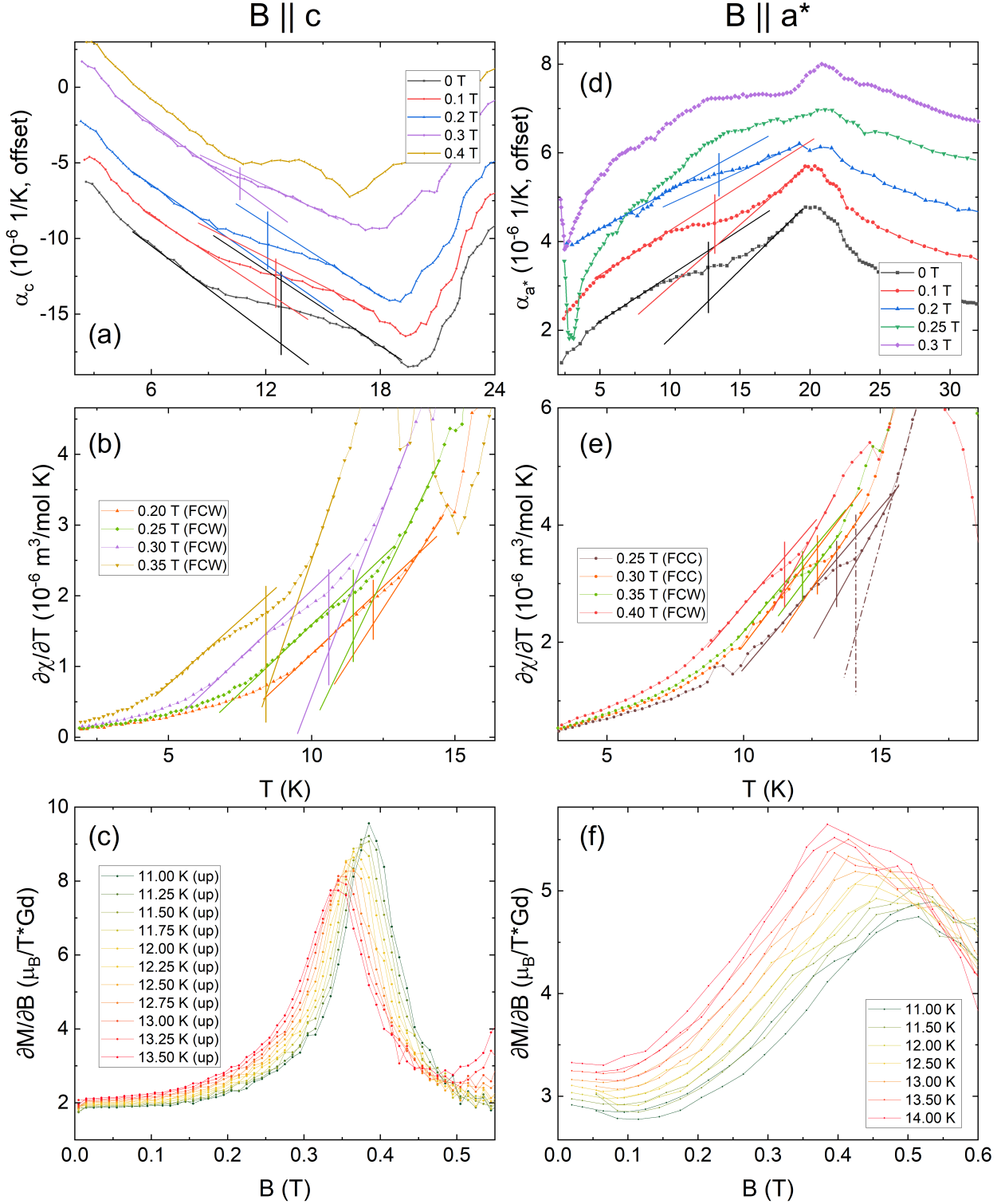


Figure S10: Extraction of T^* from thermal expansion (a, d), $\partial\chi/\partial T$ (b, e) and $\partial M/\partial B$ for $B \parallel c$ (a-c) and $B \parallel a^*$ (d-f). Vertical lines mark the position of T^* for the different measurements. Data in (a) and (d) are offset by $2 \cdot 10^{-6} 1/K$ and $1 \cdot 10^{-6} 1/K$, respectively.

IC-1/IC-1' \rightarrow A(SkL) – c -axis: Relevant quantities, entropy changes and uniaxial pressure dependencies							
T (K)	B_c (T)	$\Delta(dL/L)$ (10^{-6})	Δm (μ_B/Gd)	$\partial B_c/\partial T$ (T/K)	ΔS_{calc} (mJ/mol K)	$\partial T_c/\partial p_i$ (K/GPa)	$\partial B_c/\partial p_i$
1.77	0.52 \pm 0.02	-7.3 \pm 0.8	1.00 \pm 0.10	-0.01135	126 \pm 13	-4.1 \pm 0.6	-0.046
4.3	0.49 \pm 0.02	-10.8 \pm 1.1	0.99 \pm 0.10	-0.01133	125 \pm 13	-6.1 \pm 0.9	-0.069
5.01	0.48 \pm 0.02	-8.9 \pm 0.9	0.99 \pm 0.10	-0.01151	127 \pm 13	-4.9 \pm 0.7	-0.056
7.94	0.45 \pm 0.02	-8.4 \pm 0.9	0.95 \pm 0.10	-0.01318	140 \pm 14	-4.2 \pm 0.6	-0.056
9.83	0.42 \pm 0.02	-8.7 \pm 0.9	0.81 \pm 0.08	-0.01499	135 \pm 14	-4.6 \pm 0.7	-0.068
9.99	0.42 \pm 0.02	-7.2 \pm 0.8	0.81 \pm 0.08	-0.01516	137 \pm 14	-3.7 \pm 0.6	-0.056
12.02	0.38 \pm 0.02	-7.0 \pm 0.7	0.75 \pm 0.08	-0.01783	149 \pm 15	-3.3 \pm 0.5	-0.059
14.35	0.34 \pm 0.02	-4.5 \pm 0.5	0.52 \pm 0.05	-0.02260	131 \pm 14	-2.4 \pm 0.4	-0.055
16	0.30 \pm 0.02	-2.4 \pm 0.3	0.40 \pm 0.04	-0.02505	110 \pm 11	-1.5 \pm 0.2	-0.038
IC-3 \rightarrow IC-2 – c -axis: Relevant quantities, entropy changes and uniaxial pressure dependencies							
18.39	0.30 \pm 0.04	-9 \pm 2	0.24 \pm 0.03	-0.1	270 \pm 40	-2.3 \pm 0.6	-0.23
20.27	0.23 \pm 0.04	-3.8 \pm 0.4	0.21 \pm 0.05	-0.04	94 \pm 30	-2.9 \pm 0.8	-0.12

Table S1: Relevant quantities and jumps, calculated changes of entropy, and calculated pressure dependencies for the discontinuous transition in magnetic field from IC-1/IC-1' \rightarrow A(SkL) and IC-3 \rightarrow IC-2 for the c -axis according to Eq. (7). The column of $\partial B_c/\partial T$ was calculated by taking the derivative of a polynomial fit to the values $B_c(T)$ for IC-1/IC-1' \rightarrow A(SkL) and a linear fit (between between 18.39 K and 19 K as well as between 19 K and 21 K) for IC-3 \rightarrow IC-2.

A(SkL) \rightarrow IC-2 – c -axis: Relevant quantities, entropy changes and uniaxial pressure dependencies

T (K)	B_c (T)	$\Delta(dL/L)$ (10^{-6})	Δm (μ_B/Gd)	$\partial B_c/\partial T$ (T/K)	ΔS_{calc} (mJ/mol K)	dT_c/dp_i (K/GPa)	$\partial B_c/\partial p_i$
1.77	1.11 ± 0.03	0	0.95 ± 0.10	-0.028	300 ± 30	0	0
4.3	1.04 ± 0.03	-2.4 ± 0.3	1.01 ± 0.11	-0.031	360 ± 40	-0.47 ± 0.07	-0.015
5.01	1.01 ± 0.02	-1.4 ± 0.2	1.00 ± 0.10	-0.033	370 ± 40	-0.27 ± 0.04	-0.009
7.94	0.91 ± 0.02	-2.5 ± 0.3	0.99 ± 0.10	-0.041	450 ± 50	-0.40 ± 0.06	-0.016
9.83	0.82 ± 0.02	-5.1 ± 0.5	0.98 ± 0.10	-0.048	520 ± 60	-0.69 ± 0.10	-0.033
9.99	0.82 ± 0.02	-2.9 ± 0.3	0.98 ± 0.10	-0.048	530 ± 60	-0.39 ± 0.06	-0.019
12.02	0.7 ± 0.02	-5.9 ± 0.6	0.93 ± 0.10	-0.057	590 ± 60	-0.70 ± 0.10	-0.040
14.35	0.56 ± 0.02	-5.9 ± 0.6	0.75 ± 0.08	-0.069	580 ± 60	-0.72 ± 0.11	-0.050
16	0.45 ± 0.02	-4.0 ± 0.4	0.66 ± 0.07	-0.079	580 ± 60	-0.49 ± 0.07	-0.039
18.39	0.23 ± 0.02			-0.095			

Table S2: Relevant quantities and jumps, calculated changes of entropy, and calculated pressure dependencies for the discontinuous transition in magnetic field from A(SkL) to IC-2 for the c -axis according to Eq. (7). The column of $\partial B_c/\partial T$ was calculated by taking the derivative of a polynomial fit to the values $B_c(T)$.

A(SkL) \rightarrow IC-2 – c -axis: Relevant quantities, entropy changes and uniaxial pressure dependencies

B (T)	T_c (K)	$\Delta(dL/L)$ (10^{-6})	Δm (μ_B/Gd)	$\partial T_c/\partial B$ (K/T)	ΔS_{calc} (mJ/mol K)	dT_c/dp_i (K/GPa)
0	19.7 \pm 0.5		no SkL			
0.1	19.3 \pm 0.3		no SkL	-4.8		
0.2	18.8 \pm 0.5		no SkL	-8.1		
0.3	17.9 \pm 0.7		no SkL	-10.8		
0.4	16.4 \pm 0.4	-5.0 \pm 1.0	0.36 \pm 0.04	-13.0	310 \pm 40	-1.2 \pm 0.3
0.5	15.3 \pm 0.4	-7.4 \pm 1.0	0.54 \pm 0.04	-14.8	410 \pm 40	-1.3 \pm 0.2
0.6	13.6 \pm 0.3	-7.0 \pm 0.7	0.70 \pm 0.04	-16.0	490 \pm 30	-1.02 \pm 0.12
0.7	12.0 \pm 0.3	-5.1 \pm 0.5	0.77 \pm 0.04	-16.7	510 \pm 30	-0.70 \pm 0.08
0.8	10.4 \pm 0.3	-2.7 \pm 0.3	0.86 \pm 0.04	-17.0	560 \pm 30	-0.34 \pm 0.04
0.9	8.60 \pm 0.3	-1.3 \pm 0.1	0.91 \pm 0.04	-16.7	610 \pm 30	-0.15 \pm 0.02

Table S3: Relevant quantities and jumps, calculated changes of entropy, and calculated pressure dependencies for the discontinuous transition in temperature from A(SkL) to IC-2 for the c -axis according to Eq. (7). The column of $\partial T/\partial B$ was calculated by taking the derivative of a polynomial fit to the values $T_c(B)$, including the values from 0 T to 0.3 T.

IC-2 \rightarrow DP – c -axis: Relevant quantities, entropy changes and uniaxial pressure dependencies

T (K)	B_c (T)	$\Delta(dL/L)$ (10^{-6})	Δm (μ_B/Gd)	$\partial B_c/\partial T$ (T/K)	ΔS_{calc} (mJ/mol K)	dT_c/dp_i (K/GPa)	$\partial B_c/\partial p_i$
1.77	3.51 ± 0.05	-17.1 ± 1.7	0.08 ± 0.03	-0.04 ± 0.04	16 ± 16	-80 ± 80	-1.4 ± 0.4
4.3	3.44 ± 0.05	-12.2 ± 2	0.08 ± 0.04	-0.014 ± 0.014	7 ± 7	-130 ± 130	-0.9 ± 0.3
5.01	3.44 ± 0.10	-11.8 ± 0.4	0.07 ± 0.03	-0.008 ± 0.008	3 ± 3	-250 ± 250	-1.0 ± 0.3
7.94	3.45 ± 0.15	-6 ± 3	0.044 ± 0.018	0.018 ± 0.009	-4 ± 3	100 ± 80	-0.9 ± 0.3

Table S4: Relevant quantities and jumps, calculated changes of entropy, and calculated pressure dependencies for the discontinuous transition in magnetic field from IC-2 to DP for the c -axis according to Eq. (7). The column of $\partial B_c/\partial T$ was calculated by taking the derivative of a polynomial fit to the values $B_c(T)$.

IC-2 \rightarrow fiFM – c -axis: Relevant quantities, entropy changes and uniaxial pressure dependencies

T (K)	B_c (T)	$\Delta \lambda$ ($10^{-6}/\text{T}$)	$\Delta(\partial M/\partial B)$ ($\mu_B/(\text{T Gd})$)	$\partial B_c/\partial p_i$ (T/GPa)
9.99	3.7 ± 0.1	15 ± 2	-0.15 ± 0.03	-0.7 ± 0.2
12.02	3.0 ± 0.1	17 ± 2	-0.19 ± 0.03	-0.6 ± 0.2
14.35	2.3 ± 0.1	19 ± 2	-0.25 ± 0.03	-0.5 ± 0.1

Table S5: Relevant quantities and jumps and calculated field and pressure dependencies for the continuous transition from IC-2 to the field-induced ferromagnetic (fiFM) phase for the c -axis according to Eq. (4), (5).

DP \rightarrow fiFM – c -axis: Relevant quantities, entropy changes and uniaxial pressure dependencies

T (K)	B _c (T)	$\Delta\lambda$ ($10^{-5}/\text{T}$)	$\Delta(\partial M/\partial B)$ ($\mu_{\text{B}}/(\text{T Gd})$)	$\partial B_c/\partial p_i$ (T/GPa)
1.77	8.8 \pm 0.5	-4.7 \pm 1.0	-0.159 \pm 0.018	1.9 \pm 0.5
4.3	7.94 \pm 0.4	-1.9 \pm 1.0	-0.094 \pm 0.009	1.3 \pm 0.7
5.01	6.6 \pm 0.4	-1.4 \pm 1.0	-0.074 \pm 0.018	1.2 \pm 0.9
7.94	6.48 \pm 0.6	-0.7 \pm 0.4	-0.065 \pm 0.018	0.6 \pm 0.4

Table S6: Relevant quantities and jumps and calculated field and pressure dependencies for the continuous transition from the depinned phase (DP) to the field-induced ferromagnetic (fiFM) phase for the c -axis according to Eq. (4), (5).

IC-1 \rightarrow IC-1' – c -axis						
B	T _c	$\Delta\alpha_c$	Δc_p	$\Delta(\partial M/\partial T)$	dT_c/dp_i	dT_c/dB_i
(T)	(K)	(10^{-6})	(J/mol K)	($10^{-3}\mu_{\text{B}}/\text{f.u. K}$)	(K/GPa)	(K/T)
0	12.8 \pm 0.7	4.1 \pm 0.5	-2.7 \pm 0.5		-1.4 \pm 0.3	
0.2	12.15 \pm 0.5	2.7 \pm 0.4	-1.8 \pm 0.4	-5.6 \pm 1.4	-1.3 \pm 0.4	-0.037 \pm 0.013
0.25	11.45 \pm 0.5			-11 \pm 4		
0.3	10.6 \pm 0.5	0.9 \pm 0.3	-0.6 \pm 0.3	-16 \pm 6	-1.1 \pm 0.7	-0.28 \pm 0.18
0.35	8.4 \pm 0.5			-20 \pm 7		

Table S7: Relevant quantities, jumps, and calculated field and pressure dependencies for the continuous transition at T* from IC-1 to IC-1' for the c -axis according to Eq. (4), (5). Note that the c_p data was only measured at 0 T. The jumps in field B were scaled by the changes of the jumps in α_c , i.e., $\Delta c_p(B) = c_p(0) \cdot \Delta\alpha(B)/\Delta\alpha(0)$.